Improving a Silicon Based Triple Junction Cell for Solar Water Splitting

By

Machiel Stam

in partial fulfillment of the requirements for the degree of

Master of Science
in Sustainable Energy Technology

at the Delft University of Technology,
to be defended publicly on Thursday August 31, 2017 at 10:00 AM.

Daily supervisor:	Paula Perez Rodriguez
Supervisor:	Prof. Dr. Arno H.M. Smets
Thesis committee:	Prof. Dr. Arno H.M. Smets
	Dr. René A.C.M.M. van Swaaij
	Dr. Mohamad Ghaffarian Niasar
	Paula Perez Rodriguez

Abstract

In the transition towards a renewable based energy supply, one of the main challenges is the intermittent nature of most renewable energy sources. In order to ensure a stable energy supply, different storage technologies attract a lot of research attention. For long term storage, using hydrogen as artificial fuel is a promising option. However, in order for hydrogen storage to be renewable, the hydrogen must be produced using renewable energy. A possible option is to use solar energy to drive the electrolysis of water. In this way, hydrogen is produced directly from sunlight by driving the redox reaction with a reversible potential of 1.23 V. However, due to overpotentials and possible losses a voltage of 1.6-2 V is needed form the used device to drive the reaction. Recently, a wafer based triple junction silicon solar cell was proposed to generate the voltage needed to drive the water splitting reaction. The cell uses an n-type crystalline silicon wafer as substrate, and has an a-Si/nc-Si/c-Si structure. Although this cell demonstrates the feasibility of this technology, the performance is not good enough yet to drive the water splitting reaction efficiently.

In this work, several ways to optimize the triple junction solar cell have been studied. First, optimising the tunnel recombination junctions improves the open circuit voltage of the device. For the tunnel recombination junction between the top a-Si and the middle nc-Si cell, this is done by using a combination of a thin n-SiO_x layer and a thin n-a-Si layer. Apart from a small improvement in optical performance this configuration improves the conductivity of the junction and also slightly enhances charge separation and collection in both sub-cells. For the junction between the middle nc-Si and the bottom c-Si cell, the same result was achieved by increasing the doping in the n-layer. Subsequently, to improve current matching of the device, the nc-Si layer thickness can be increased to 3500 nm without sacrificing the electrical performance. In addition, optimizing the interface between the top p-nc-SiO_x layer and the front transparent conductive oxide (TCO) also improves the electrical performance of the device. Moreover, it was found that using hydrogenated indium oxide as front TCO instead of indium doped tin oxide increases the current by decreasing the reflection in the wavelength region of the current limiting nc-Si middle cell by having reflection, and also increases the open circuit voltage of the device by 0.3 Volts. The final triple junction cell achieved an open circuit voltage of 1.93 V and a short circuit current density of 8.5 mA/cm^2, with a fill factor of 0.65. With these improvements, it is estimated that a solar to hydrogen efficiency of 6.2 % can be reached by using an IrO_x counter electrode.

Table of Contents

List of figures

List of tables

Nomenclature

3j	Triple junction
a-Si	Amorphous silicon
Ag	Silver
Ar	Argon
Al	Aluminium
AZO	Aluminum doped zinc oxide
BSF	Back surface field
c-Si	Crystalline silicon
CVD	Chemical vapour deposition
Cr	Chromium
EQE	External quantum efficiency
FF	Fill factor
FZ	Float zone
IrO_x	Iridium oxide
ITO	Indium tin oxide
J_{sc}	Short-circuit current density
MJ	Multijunction
NAOC	Nitric acid oxidation cycle
nc-Si	Nanocrystalline silicon
$nc\text{-}SiO_x$	Nanocrystalline silicon oxide
η	Efficiency
PECVD	Plasma-enhanced chemical vapour deposition
PVD	Physical vapour deposition
RF	Radio frequency
R_s	Series resistance
R_{sh}	Shunt resistance
SHJ	Silicon heterojunction
STC	Standard Test Conditions
TCO	Transparent conductive oxide
TF	Thin film
TRJ	Tunneling recombination junction
V_{mpp}	MPP voltage
V_{oc}	Open-circuit voltage

1. Introduction

As agreed by the 2015 Paris agreement, it is crucial to keep the global average temperature increase below 2 °C. In order to achieve this long-term temperature goal, each country is obliged to reduce greenhouse gas emissions. A significant portion of CO_2 emissions originate from electricity production from non-renewable fuels [1]. Recognizing this, many counties pledged to increase the renewable share of their electricity production. The International Energy Agency (IEA) prospects in their world energy outlook 2016 that 60% of the new electricity generation capacity in the coming 20 years will be renewable [2], where solar energy together with wind energy will be responsible for half of this growth. Figure 1 shows the global electricity generation by source for 2014 and the expected values for 2040.

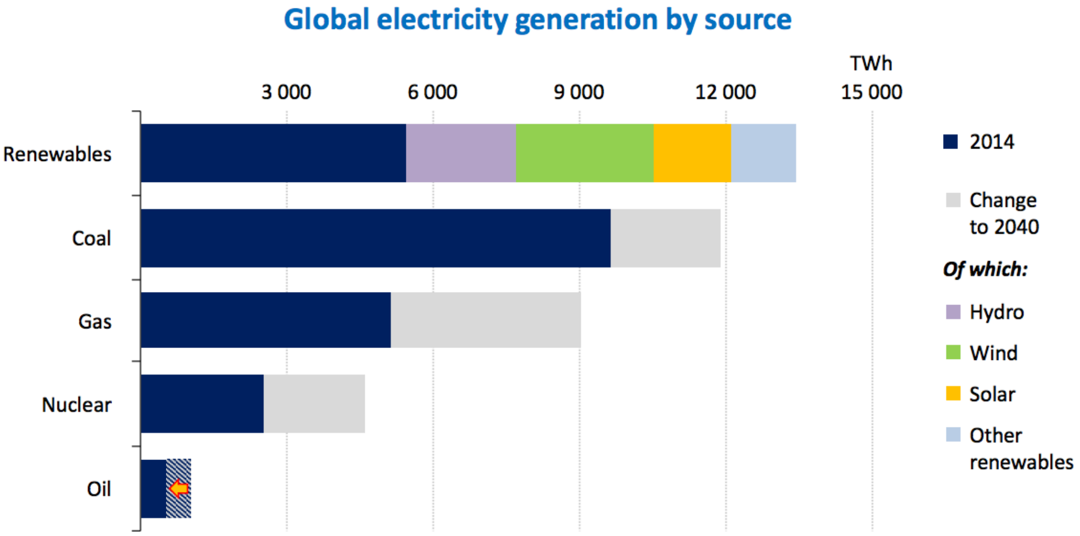

Figure 1: Global electricity generation by source in 2014 and expected generation in 2040 [3]

A disadvantage associated with these renewable energy sources is that the electricity production of solar panels and wind turbines is highly dependent on the weather conditions. It is evident that Solar PV can only produce electricity at times when the sun is shining, and thus no or little production will happen at night and in the winter months. Regarding wind energy sources, the average wind speed shows a diurnal cycle, where the average wind speeds 2-3 hours before sunset can be 2-3 times larger than the average wind speeds just before sunrise [4]. In addition to the daily variations, there are also huge seasonal variations. Figure 2 shows the capacity factor for different renewable energy technologies over a 34 month period in the US. It can be seen that especially the capacity factor for solar (PV and thermal) energy is hugely variable throughout the year. With the current state of the energy mix, fossil fuel combustion plants can adapt to the variation in renewable energy generation, but with an increasing penetration of renewable electricity generation, these daily and seasonal variations give rise to a need for large scale energy storage [2].

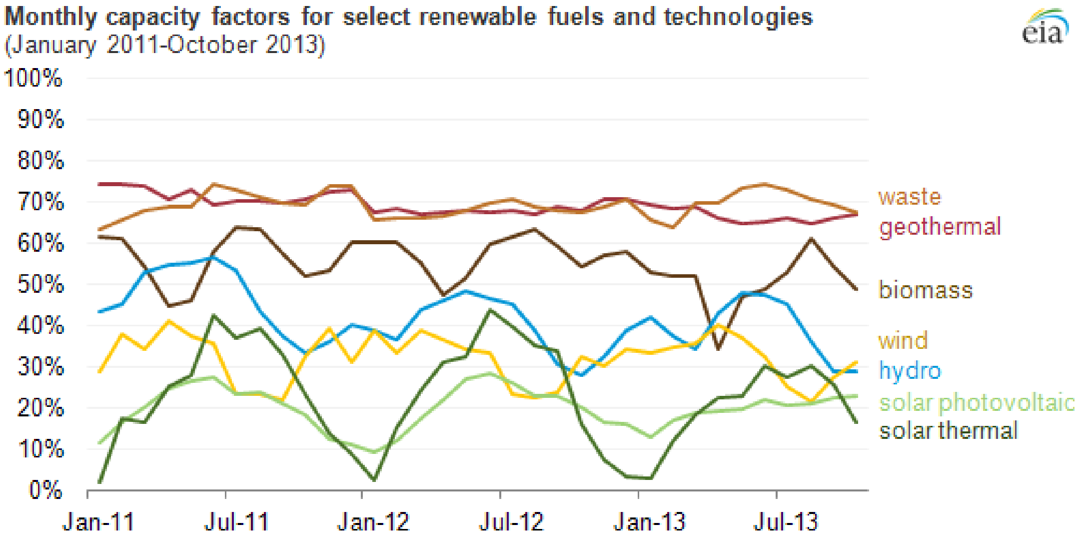

Figure 2: Monthly capacity factors for different renewable energy technologies in the US [5]

It is possible to distinguish between two main types of energy storage: short term to level daily fluctuations and long term to balance out the seasonal variations [6]. For short term storage, techniques like batteries, heat storage or compressed air energy (CAE) can be used, but for long term energy storage currently only large scale hydro plants, biomass and (artificial) fuels are a viable option [7]. Considering that large scale hydro plants are highly dependent of the geographic situation and using biomass on this large scale would compete heavily with agricultural land use [6], a good alternative is to use the excess electricity for production of an artificial fuel, which can be converted back to electricity in case of high electricity demands [8]. Carbon containing fuels would suffer from the huge entropic cost when taking CO_2 out of the atmosphere due to the high dilution [9]. Hydrogen is therefore a promising fuel to balance out electricity generation and consumption. Hydrogen stored as metal hydride is, together with ammonia, one of the few energy storage options that can approach both the volumetric and gravimetric energy density of fossil fuels. Moreover, upon combustion it only releases H_2O into the atmosphere.

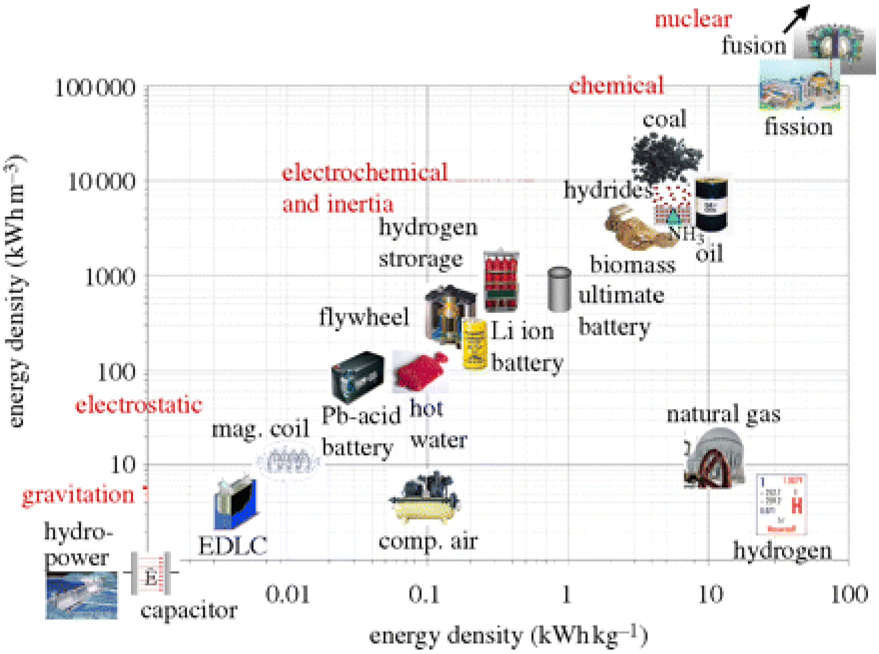

Figure 3: A plot of the volumetric versus the gravimetric energy density for several storage technologies [10]

At the moment hydrogen is mostly produced via steam reforming of methane [8]. However, for a sustainable artificial fuel, a process which does not use any type of fossil fuel is required. Hydrogen can be produced from water (water splitting) by means of electrolysis. Electricity (solar or wind) is then used to power an electrolyser to generate hydrogen. A more integrated approach is a direct photoelectrochemical (PEC) device, where sunlight is used to drive the electrochemical reaction that converts water into oxygen and hydrogen gas [11]. Due to the (over)potential needed to drive the reaction, an operating voltage exceeding 1.6 V is needed.

In order for a hydrogen producing device to be an asset in the transition towards greenhouse gas neutral fuels it needs to be cheap and use materials that allow for mass production. Devices that produce hydrogen efficiently are up till now mostly made out of III-V semiconductor materials [12]. Two major drawbacks in using these technologies are the related costs and the scarcity of the materials. As an alternative, a triple junction solar cell based on silicon materials is proposed in this thesis to reach the required operational voltage. The limiting factor in this case would be the current density at the operational point, which is too low for efficient hydrogen production. This work investigates methods to improve the performance of the solar cell in order to achieve a higher current density at the operational point of the device.

1.2 Outline

This thesis is divided into five chapters. After having introduced the subject in chapter one, chapter two will explain the theory behind solar radiation, photovoltaic cells and photoelectrochemistry (PEC). In addition, the device and research objectives for this thesis will be discussed. Chapter three will introduce the fabrication methods and experimental analysis used to characterise the solar cells. Chapter four will display and discuss the results. Finally, in chapter five conclusions will be drawn and some recommendations will be given for further research.

2. Theoretical background

In the conversion of solar energy into an energy carrier suitable for storage, in this case hydrogen, two main steps are taking place. The first step is the conversion of photons to electricity in the form of separated charge carriers, and the second step is the utilisation of these charge carriers to drive the electrochemical water splitting reaction. These steps will first be explained separately in this section.

2.1 Solar radiation

The concept of solar energy starts with our personal star, the sun. Inside the sun, the extreme pressures and temperatures cause a nuclear fusion reaction in which mass (*m*) is converted to energy (*E*) as a proportion of the light speed at vacuum (*c*) according to the well-known formula

$$E = mc^2 \tag{1}$$

which causes an enormous heat generation inside the sun's core. At the surface, much of this energy is emitted as electromagnetic radiation. The energy of electromagnetic waves is quantized, where the energy each photon carries is wavelength dependant according to

$$E_{ph} = \frac{hc}{\lambda} = hf \tag{2}$$

where h is the Planck constant, c the speed of light in vacuum, λ the wavelength and f the frequency of the photon [13]. The emitted spectrum of photons matches closely with that of a black body radiator of almost 6000 K, as shown in Figure 4. Although just a small fraction of the generated energy reaches the outside of earth's atmosphere, the total irradiance just outside the earth's atmosphere is still 1361 W/m^2 on a plane perpendicular to the sun. This value is also called the solar constant [14]. While passing through the atmosphere to reach the earth's surface, some of the photons are absorbed, decreasing the total irradiance and changing the spectral irradiance reaching the earth. The amount of atmosphere the sunlight needs to cross, commonly referred to as Air Mass (AM), depends highly on the position of the sun, according to equation 3:

$$AM = \frac{L}{L_0} \approx \frac{1}{\cos z} \tag{3}$$

where L is the path length through the atmosphere, L_0 is the path length normal to the earth's surface and z is the zenith angle in degrees [15]. The AM0 spectrum represents the solar spectrum before passing through the atmosphere, and the AM1 spectrum is the solar spectrum incident on a flat surface if the sun is right above the earth. The standard for testing solar cells and panels for terrestrial use is the AM1.5 spectrum, corresponding to a zenith angle of 41.81 °, as defined by the American society for Testing and Materials (ASTM) and the PV industry with a spectral irradiance as shown in Figure 4 [16]. The total irradiance of an accurate AM1.5 spectrum as defined by the standards is 964W/m^2, for ease of calculation the spectrum is scaled such that the total irradiance is 1000 W/m^2.

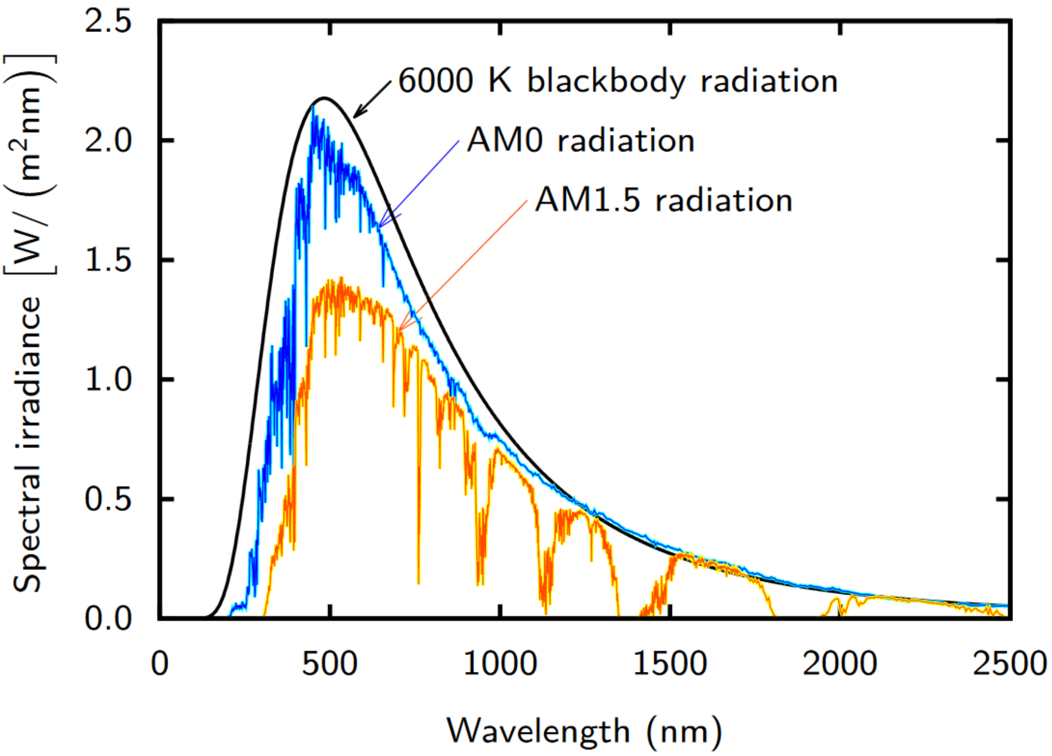

Figure 4: The spectral irradiance of the sun just outside earth's atmosphere (AM0) and after traveling through air for a distance 1.5 times the thickness of the earth's atmosphere (AM1.5)

2.2 The photovoltaic effect

The photovoltaic effect is the effect in which electromagnetic radiation induces a voltage across an electrode. Although it was first discovered by Becquerel in 1893 with an electrode immersed in an electrolyte solution, it took until 1954 for the research towards using this photoelectric effect as an energy source to take off [17]. The effect is due to the electrical band structure of materials which will be explained first.

2.1.1 Energy bands

According to quantum mechanics the energy states of electrons around an atom are quantized, with energy gaps between each allowed energy level. When two atoms are coming close together their energy levels interact to form new energy levels, and if they share their electrons a chemical bond is formed. In a crystalline solid, the energy levels for many atoms start interacting with each other due to the low interatomic distance. This causes the formation of allowed energy bands, separated by bands of forbidden energies [18].

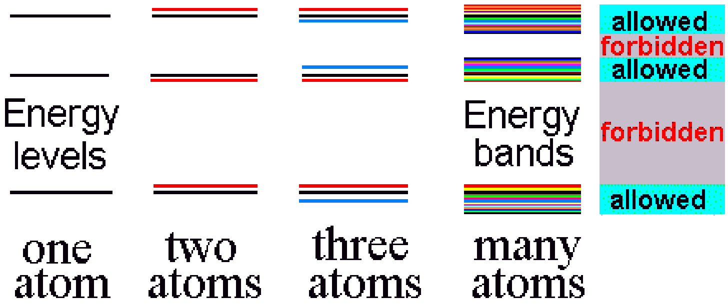

Figure 5: The interaction of energy levels. [19]

The outer electrons of all atoms share the formed energy bands, thus filling the energy bands with electrons. Whether the formed solid acts as a conductor (mostly metals) or as an insulator or semiconductor depends on the way the energy bands are occupied. In materials where electrons can hop to an empty energy level easily, charge transfer is much easier than in materials where electrons fill the bands completely. To understand the way electrons fill the energy bands, a closer look at the Fermi level is needed. The Fermi energy is the electrochemical potential of electrons and defines the highest energy levels occupied by electrons at absolute zero temperature. At non-zero temperatures, energy levels around the Fermi level show an electron distribution according to the Fermi-Dirac equation:

$$f(E) = \frac{1}{e^{(E-Ef)/kT}+1} \tag{4}$$

where *f(E)* gives the probability for energy level *E* to be occupied by an electron, E_f is the energy of the Fermi level and *kT* the thermal voltage. An energy level with the same energy as E_f has a 50% chance of being occupied by an electron.

As shown in

Figure 6 there are three main types of Fermi level positions. For metals and conductors, the Fermi level lies in an allowed energy band, which means that the electrons around the Fermi level can easily move around in the material by hopping to the unoccupied energy states. For insulators, the Fermi level position lies in a forbidden energy band with an energy difference so high that there are virtually no electrons in the conduction band and no unoccupied energy levels in the valence band. This makes charge transfer difficult, because electrons need to overcome the large bandgap in order to be exited towards the conduction band and conduct charge. In a semiconductor, the Fermi level lies in a forbidden energy gap with less energy difference, which gives some electrons the possibility to cross the forbidden energy band and conduct electricity while moving around in the conduction band. These electrons leave behind empty spaces in the valence band where an electron should be. The missing negative charge of the electron gives rise to a positive charge which can move through the material if a neighbouring electron hops into the empty space. This empty space is therefore treated as a quasi-particle called hole, with a charge of equal magnitude but opposite sign compared to an electron [18].

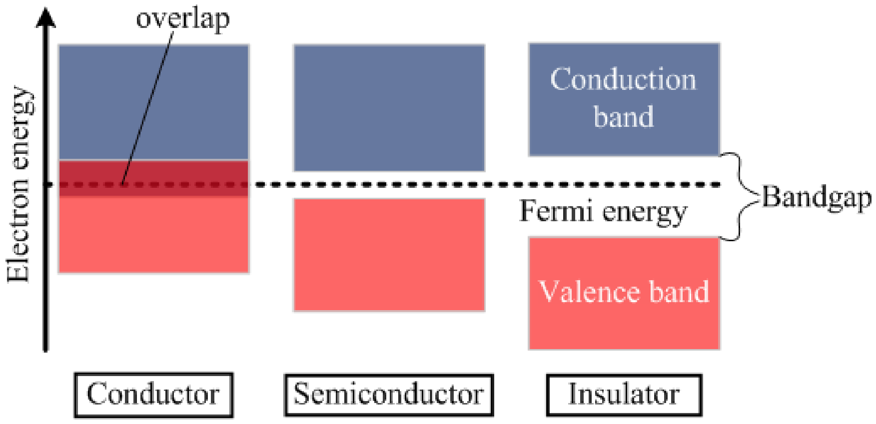

Figure 6: Fermi level position for conductors, semiconductors and insulators [20]

2.1.2 Charge carrier generation

When a semiconductor material is illuminated, photons can excite the electrons to a higher energy level, corresponding with the energy that the photon contains. The electron leaves behind an empty state in the valence band, a hole. Illumination thus increases the amount of electrons in the conduction band and the amount of holes in the valence band. But not all photons will contribute to charge carrier generation. Only if a photon has an energy equal to or higher than the band gap of the semiconductor material it can be absorbed to generate an electron hole pair. Less energetic photons will generally pass through the material without being absorbed. Photons with more energy than the band gap energy will excite the electrons to positions above the conduction band edge, but the charge carriers quickly fall back to the band edge while generating heat in a process called thermalisation, as shown in Figure 7.

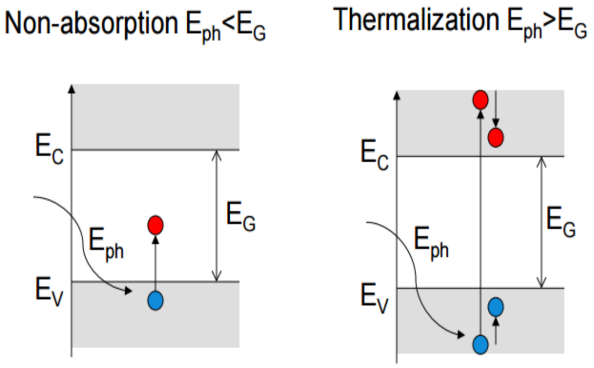

Figure 7: Non-absorption and thermalisation losses

The total energy that can be utilised by a single junction solar cell is limited by these two phenomena. When using a low band gap semiconductor material more photons can be absorbed. However, the amount of energy that can be utilised from each photon is only dependent on the operating voltage of the device, which is generally lower for a low band gap material. The remaining photon energy is lost by thermalisation and the device will have a low V_{oc}. When using a high band gap semiconductor material on the other hand, the thermalisation losses are reduced, but a larger fraction of the spectrum will not be absorbed, so the device will have a low J_{sc}.

It is possible to calculate the theoretical efficiency limit of a solar cell with a single p-n junction, the Shockley-Queisser limit. This is the efficiency of an ideal solar cell, with radiative recombination as only recombination mechanism [21]. Figure 8 shows a plot of the maximum efficiency versus the band gap of the semiconductor material used.

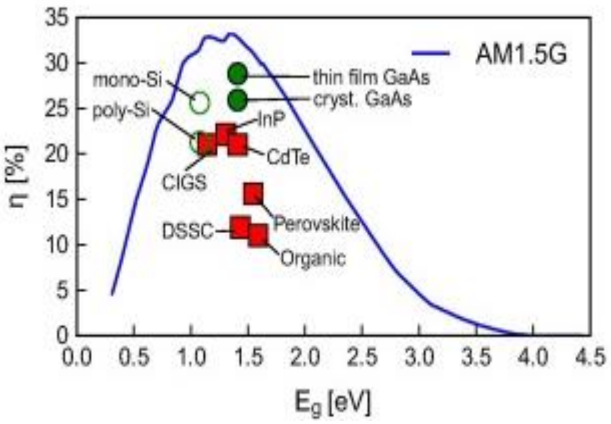

Figure 8: The Shockley-Queisser limit as a function of bandgap [22].

The curve is not completely smooth due to atmospheric absorption, and shows two local maxima. At a band gap of 1.34 eV lies the global maximum, with a theoretical efficiency of 33.16%. Crystalline silicon, with a band gap of 1.12eV, has a theoretical efficiency limit of 32.23%. Using multi-junction technologies the spectral utilisation can be improved by absorbing short wavelength light with a larger bandgap semiconductor and long wavelength light with a smaller bandgap semiconductor. The efficiency limit increases to 42 % for tandem junction cells, and to 49 % for triple junction cells [23].

In the calculation for the Shockley-Queisser limit it is assumed that all incoming photons are absorbed by the solar cell. The absorption coefficient of the absorber material determines for a large part how thick the solar cell should be in order to absorb (almost) all photons. For example, amorphous silicon (a-Si)has a high absorption coefficient and a-Si cells mostly have a thickness of several hundreds of nanometres. The same is true for solar cells based on III-V technology. On the other hand, crystalline silicon (c-Si) has a low absorption coefficient due to its indirect band gap. This means that the top edge of the valence band does not align with the bottom edge of the conduction band. In order to excite an electron from the valence to the conduction band in an indirect band gap semiconductor, momentum must be supplied by a phonon (lattice vibration). This lowers the absorption coefficient of the material, and when using c-Si to make solar cells, a wafer of a few hundreds of micrometres is needed to absorb all light efficiently.

2.1.3 Charge carrier separation

The generation of charge carriers on itself is not enough to produce electricity. In order for current to flow, these charge carriers need to be separated, so that at one terminal the electrons can be collected and at the other terminal the holes can be collected. There are two main mechanisms of charge carrier transport inside a semiconductor. The first one is drift, where an electric field separates electrons and holes because holes are accelerated in the direction of the field, whereas electrons are accelerated against the direction of the electric field. Inside a solar cell an electric field is created in the depletion region, which will be explained further in the following sections. Charge carriers generated within the depletion region will be separated by the electric field. The second transport mechanism is diffusion. Diffusion separates the electron hole pair with the help of a concentration gradient. Charge carriers generated outside the depletion regions will only be separated if the minority charge carriers diffuse towards the electric field before they recombine. This limits the total effective thickness of an absorbing layer to the depletion region thickness plus the minority charge carrier diffusion length.

The diffusion length is directly related to the purity and quality of the semiconductor material. Imperfections in a crystal structure, impurities and grain boundaries provide recombination sites, lowering the diffusion length. As stated earlier, c-Si solar cells are relatively thick due to the low absorption coefficient. To ensure a long enough diffusion length the material should be of ultrahigh purity, up to 99.9999999% [24]. This makes the high efficiency crystalline silicon solar cells relatively expensive.

For charge collection, the n and p side of the device need to be connected externally so that the current can flow. The potential difference between the two sides can be used directly as electricity (regular PV) or to drive an electrochemical reaction (PV electrolysis, PEC cells). The metal contact points are mostly made of aluminium or silver. A general disadvantage of the metal contacts is that they not only provide electronic connection, but also recombination sites at the contacts due to the material interface. Therefore passivation is required to reduce the recombination losses. It depends on the solar cell technology which passivation strategy is being used [25].

2.1.4 Doping

In an intrinsic semiconductor, the Fermi level lies in the middle of the band gap, because the chance to find an electron at that (hypothetical) energy level is 50%. This position can be changed by adding impurities to the material, also called doping. By doping the material, separation of charge carriers can be enhanced. An n-type semiconductor is doped with donor atoms that have one valence electron more than the atom they replace. The donor atom is chosen in such a way that the energy level of the donor atom is just below the conduction band edge. Electrons can then easily be exited to the conduction band and diffuse through the crystal lattice, while the donor atom cannot do so. This means that there are more electrons in the conduction band for an n-type material, shifting the Fermi level upwards with reference to the conduction band. A p-type semiconductor, on the other hand, is doped with acceptor atoms that have one valence electron less, giving rise to additional holes in the conduction band. This is illustrated in Figure 9.

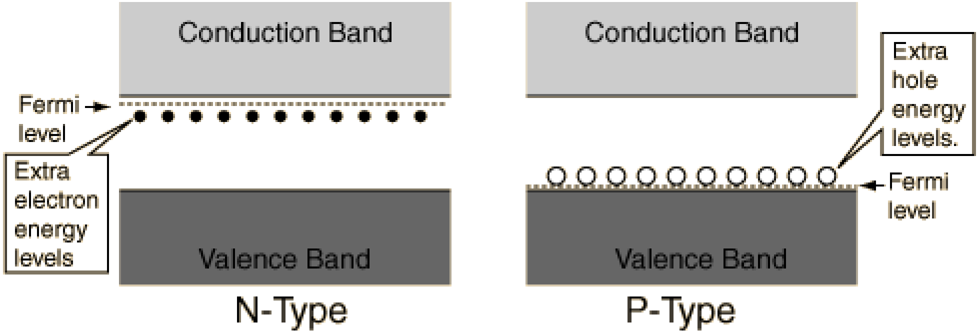

Figure 9: Energy bands for an n-type (left) and p-type (right) semiconductor [26]

In silicon semiconductors boron is mostly used as acceptor and phosphorous as donor. Note that the semiconductor material as a whole is still neutral, but the charge carriers can move around freely in the material, while the dopant atoms cannot.

2.1.5 p-n junctions in the dark

If p- and n-type silicon are brought into contact with each other the excess holes from the p region diffuse into the n region and excess electrons from the n region diffuse into the p region, where they recombine. This leaves the fixed donor and acceptor atoms with their charge no longer counterbalanced by the mobile charge carriers. The charged atoms generate an internal electric field at the junction, called a depletion region (because it is depleted of free charge carriers). Equilibrium is established when the electric field is equal but opposite to the diffusion of charge carriers, so that there is no net charge transfer. If equilibrium is established, the Fermi level is constant throughout the junction.

Thus, in a p-type material the Fermi level lies close to the valence band, in an n-type material the Fermi level lies close to the conduction band. As a result the conduction and valence band show band bending within the p-n junction, corresponding with the potential difference across the electric field of the p-n junction. It should be noted that the horizontal axis in Figure 10 is not to scale, generally the p-type base of a silicon solar cell is much wider than the n-type side, and the total wafer is around 100 times wider than the p-n junction [27].

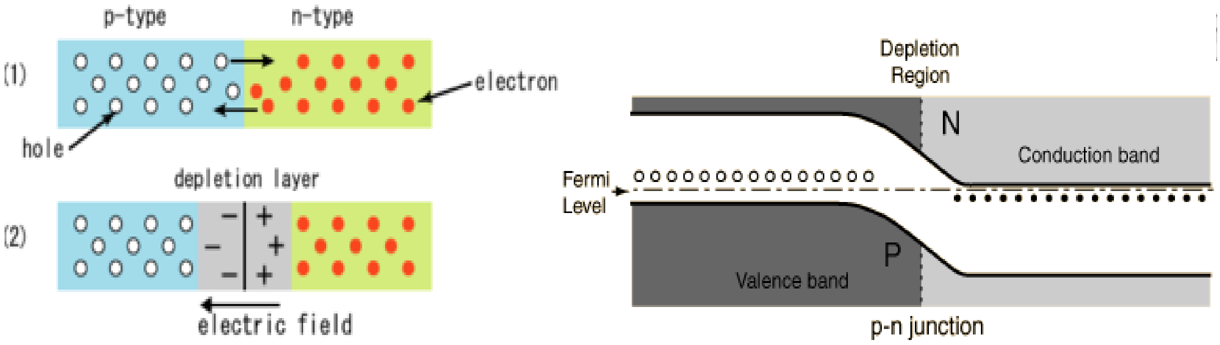

Figure 10: Formation of a p-n junction (left) and the corresponding band diagram (right) with the fixed dopant atom energy levels.

2.1.6 Illuminated p-n junction

Apart from the influence of doping on the Fermi level position, the generation of charge carriers by illumination also changes the Fermi level position. As explained before, illumination increases both the number of electrons in the conduction band and the number of holes in the valence band. The generated charge carriers cause what is called quasi Fermi level splitting. The increased number of electrons in the conduction band would move the Fermi level closer towards the conduction band. On the other hand the increased number of holes would move the Fermi level closer towards the valence band. This means that the Fermi levels for electrons and holes are not equal, but both electrons and holes establish a quasi-equilibrium with the conduction and valence band, with the corresponding quasi-Fermi levels E_{fn} and E_{fp}.

If no external connection is made, the pn junction is operating under open circuit conditions, shown in Figure 11 on the left. The energy difference between E_{fn} and E_{fp} divided by the elementary charge is equal to the open circuit voltage, V_{oc}. This is the voltage at which no current is flowing, and the maximum voltage that can be obtained from a solar cell. If the pn junction is externally short circuited E_{fn} at the n side aligns with E_{fp} of the p side, shown in Figure 11 on the right. In this situation the voltage is applied internally over the pn junction to ensure maximum separation of charge carriers, giving the highest current a solar cell can produce. This is called the short circuit current, J_{sc}.

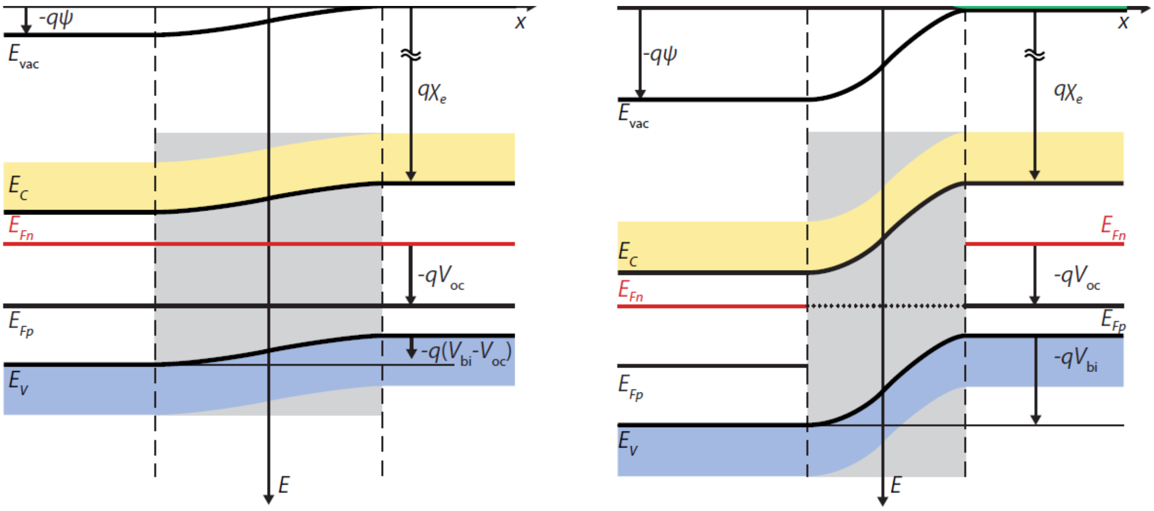

Figure 11: Illuminated p-n junction under open circuit (left) and short circuit (right) condition [28].

2.1.7 p-i-n junction

Thin film silicon cells cannot achieve efficient solar cell operation the same way as c-Si technology. These films have a higher absorption coefficient, meaning that a much thinner layer can be used to absorb all light. Generally in the order of a few hundreds of nanometres for amorphous silicon, and a few micrometres for nanocrystalline silicon. However, the minority charge carrier diffusion length is generally very short, due to the high number of defects and dangling bonds in the material. This is especially true for doped layers, as doping severely degrades the lifetime and mobility of minority carriers in amorphous silicon. Thus, a p-n structure as with crystalline silicon cannot be used in the same way for these materials. Instead of diffusion, drift should be used as the main transport mechanism for charge carriers.

The solution is found by constructing a p-i-n junction. An intrinsic absorber layer is sandwiched between two thin doped layers, and the electric field generated by the p-n junction is 'stretched out' over the intrinsic layer in the middle. This can be seen by the slope of E_c and E_v in Figure 12. This means that throughout the complete absorber layer, charge carriers experience the electric field, and will be separated more efficiently [29]. The low minority carrier mobility in the doped amorphous silicon is now an advantage. Charge carrier generation happens in the intrinsic absorber layer, and the doped layers function as carrier selective contacts, meaning they only let the majority carriers pass through, while rejecting the minority carriers due to their low mobility [30]. Although p-i-n junctions improve charge carrier separation for solar cells with short diffusion lengths, this structure is only beneficial over p-n junctions if the short diffusion length of a semiconductor material requires so. For high diffusion length semiconductors a pn-junction gives a higher V_{oc} and Fill Factor [27], [30].

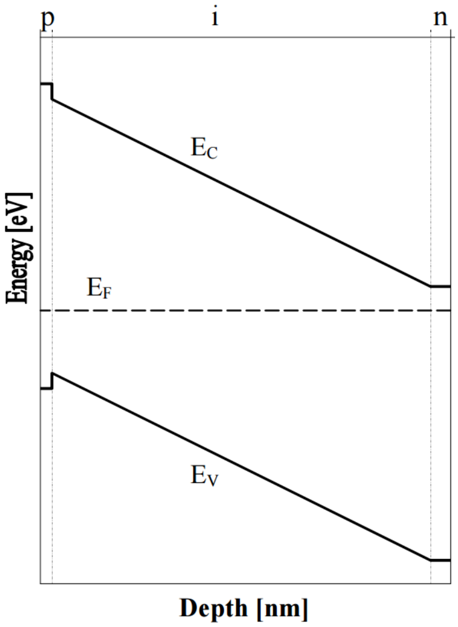

Figure 12: Schematic energy band diagram for a p-i-n junction

2.3 Photovoltaic technologies

There are different PV technologies with different strengths and drawbacks. The III-V technologies, constructed from materials in group III and V of the periodic table of elements, have the highest overall efficiencies and exhibit superior performance to all other technologies. They have a direct band gap and excellent electronic properties. A drawback is that manufacturing the solar cells is relatively expensive due to expensive deposition techniques and low abundance of the elements (Ge, Ga, As). This is the reason why they are mainly used in space applications [31] and concentrator solar photovoltaics [32]. The commercial solar cell industry is based on 3 ‘materials’, namely Si, CdTe and CIGS. Of these, CdTe and CIGS both have a relatively small market share. Based on the availability of materials (mainly gallium, indium and tellurium) it is not to be expected that these technologies can keep up with the massive growth in production that is required the coming years for a carbon-free energy market [33].

The silicon market consists of three main categories. Single crystal (or monocrystalline) cells, multicrystalline cells and thin film (TF) cells. Monocrystalline silicon cells exhibit the highest efficiency both on lab and module scale. In spite of the cost decrease due to more efficient production processes, the high costs of producing the single crystal wafers holds this technology back from dominating the market [33]. Multicrystalline cells have the advantage of cheaper fabrication compared to monocrystalline cells, but generally have lower efficiencies due to the grain boundaries inside the cells, lowering the V_{oc}. Nevertheless, their low price per watt peak (Wp) has caused them to be the dominating technology globally, and in 2015 more than 60% of the global PV panel production was multicrystalline cells [34]. Thin film silicon cells exhibit the lowest efficiencies of all commercially available PV modules, but their low cost due to low material use and ease of manufacturing keeps the technology interesting [35]. Moreover, multi-junction cells from thin film silicon technologies utilise the spectrum more efficiently, and triple junction thin film silicon modules have shown more than 10% efficiency [31]. Thus, although efficiencies of TF modules generally are much lower than that of modules based on wafer technology, the price per watt peak (W_p, the module output at reference conditions) can be lower [36].

In this project, a multi junction solar cell is constructed, consisting of a silicon heterojunction solar cell, a nanocrystalline silicon solar cell and an amorphous silicon solar cell. These materials were chosen due to their flexibility of design and relatively high efficiencies and spectral utilization. Thus, the following sections will take a closer look at these technologies and the multi-junction concept.

2.3.1 Thin film silicon solar cells

As stated earlier, silicon thin film solar cells are made in p-i-n (or n-i-p) structure. In this structure the intrinsic middle layer is the absorbing layer, and the p and n layers provide an electric field that stretches across the intrinsic middle layer to get good charge carrier separation. The n and p layers should be as thin as possible to reduce parasitic absorption. TF silicon solar cells can be made either of amorphous silicon (a-Si) or nanocrystalline (nc-Si) silicon, which is sometimes also referred to as microcrystalline silicon (μc-Si)

Amorphous silicon is a type of silicon without a long-range order. For crystalline silicon every atom forms a covalent bond with four neighbours, with a constant bond angle and length. The lack of long-range order in amorphous silicon gives rise to a high number of silicon atoms which cannot form 4 bonds, leaving a lot of ‘dangling bonds’. These dangling bonds are defect states within the band gap of amorphous silicon and need to be passivated in order to make a working solar cell [37]. Therefore amorphous silicon is hydrogenated during the film deposition, and the hydrogen passivates most of the dangling bonds. The material properties can be tuned by changing the amount of hydrogen dilution during deposition [38]. Hydrogenated amorphous silicon (a-Si:H) has a band gap of around 1.75 eV (this can be tuned slightly by varying deposition conditions) and is a direct band gap material. This allows for a much thinner absorber layer, generally in the order of a few hundreds of nanometres [29]. A major problem of amorphous silicon solar cells is the so called Staebler-Wronski effect. Under influence of light, additional defects are formed inside the material which provides extra recombination sites and lowers the conductivity of the material [39]. The effect is more prominent in thicker amorphous silicon layers [40], and in combination with the high bandgap this makes amorphous silicon a material which is less suitable for single junction solar cells. It is mainly used as a top cell in multi-junction concepts.

Nanocrystalline silicon can be considered as a transition between amorphous silicon and crystalline silicon. A nanocrystalline silicon film consists of small grains of crystalline silicon embedded within amorphous silicon. The material shows mixed phase behaviour in its optical properties. The crystalline grains inside the material have, just like crystalline silicon, an indirect band gap of around 1.1 eV, and the amorphous matrix has a direct band gap in the region of the bandgap of amorphous silicon [41]. Because the crystalline grains have an indirect band gap, a thicker layer of nanocrystalline silicon is needed for an efficient solar cell compared to amorphous silicon [42].

The material can be characterised with help of the crystalline volume fraction of the deposited film. Figure 13**Error! Reference source not found.**shows an overview of nc-Si with a decreasing crystallinity. At the far left, the material becomes polycrystalline silicon and, at the far right, amorphous silicon. The crystal grains of the material allow for a higher electron mobility compared to amorphous silicon. The band gap is around 1.1 eV, the same as that of crystalline silicon. It is an indirect band gap material, so the absorption coefficient is low compared to a-Si:H. This means that a thin film solar cell from nc-Si requires a thicker absorber layer compared to an a-Si:H solar cell., commonly in the order of a few microns. An advantage of nc-Si:H cells is that they do not suffer from degradation by the Staebler-Wronski effect. Thin film nc-Si:H solar cells are made in the same p-i-n or n-i-p structure as a-Si:H solar cells, with the intrinsic middle layer as the absorber layer.

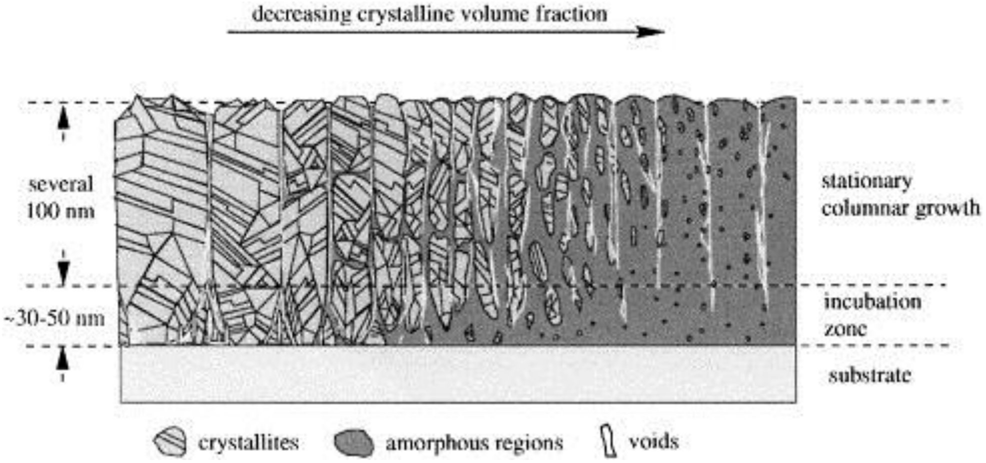

Figure 13: Schematic diagram showing nc-Si with different crystallinity. [43]

Within research towards thin film silicon solar cells, different types of n and p layers have been used. The first option is to construct a homojunction, with n- and p-type layers from the same material as the absorber layer. However, to prevent parasitic absorption and enhance carrier selectivity often materials with wider bandgaps are used, such as silicon carbide or silicon oxide. Nanocrystalline silicon oxide layers consist of a mixed phase of Si nanocrystals within an amorphous silicon oxide matrix is formed. This mixed phase allows for a high enough conductivity while at the same time giving the possibility to tune the bandgap and refractive index of the layers so that parasitic absorption losses are minimised [44].

2.3.2 Silicon heterojunction solar cells

Silicon heterojunction (SHJ) solar cells, or Heterojunction cells with Intrinsic Thin layer (HIT), are a relatively new concept with high performance [45]. As stated earlier, the front and back contact points of solar cells provide possible recombination sites. Also, recombination sites are present at the wafer edge due to the crystal boundary with its dangling bonds. To prevent this recombination the wafer edge needs to be passivated, and the minority carriers should be kept away from the contacts. In the HIT structure, this is achieved by passivating the crystalline silicon wafer (Eg = 1.1 eV) with a thin layer of amorphous silicon (Eg = 1.6-1.9 eV), and using thin layers of p- and n-type amorphous silicon to make the carrier selective contacts. A general cell structure of a textured HIT cell is shown in Figure 14, with the corresponding band diagram on the right [46].

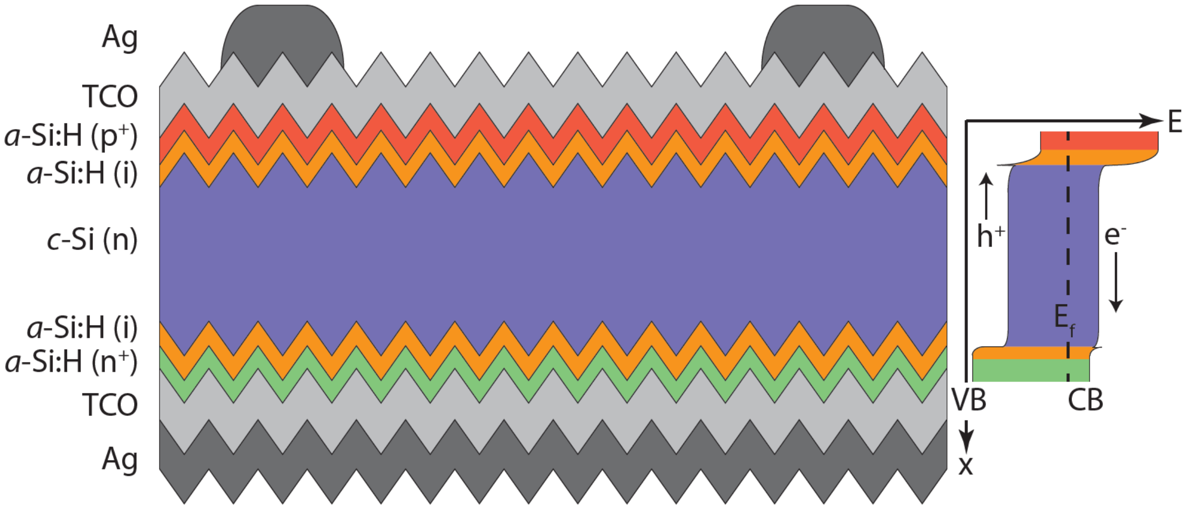

Figure 14: a textured silicon heterojunction cell and its band diagram (rotated) [47]

This structure enables passivation of the silicon wafer surface without the need for high temperature or photolithographic processes [46]. The intrinsic amorphous silicon passivates dangling bonds at the wafer edge, which reduces the number of recombination sites. Also, the front a-Si:H(p^+) and the back a-Si:H(n^+) provide the front and back surface field which reduce recombination by keeping the minority carriers away from the high recombination contact points [48]. The symmetrical structure of silicon HIT cells with intrinsic amorphous silicon passivation layers on both sides allows for a high open circuit voltage (V_{oc}) compared to conventional silicon wafer technology [45], which makes it an interesting technology for designing a high voltage triple junction cell. The highest V_{oc} values are obtained for flat wafers, texturing the wafers for light trapping purposes increases recombination at the a-Si/c-Si interface, and reduces the V_{oc} and fill factor (FF). As a result there is a trade-off between J_{sc} and V_{oc} for these cells [49].

2.3.3 Multijunction solar cells

As mentioned earlier, solar cells suffer from efficiency loss due to thermalisation and non-absorption of photons. This limits the theoretical maximum efficiency for a c-Si solar cell to 32%. A possible way to deal with this problem is to use a stack of solar cells on top of each other, called a multijunction solar cell. By using semiconductor materials with different band gaps, a bigger part of the spectrum can be utilised efficiently, as shown in **Error! Reference source not found.**. The gain in aximum theoretical efficiency from using a multijunction solar cell can be calculated in a similar way as the Shockley-Queisser limit was calculated for a single junction solar cell. With an optimal band gap configuration the efficiency limit is 42% for a double junction solar cell and 49% for a triple junction solar cell [50]. Of course, these values are not achieved due to several loss mechanisms. The record efficiency is 37.9% for a triple junction III-V cell, and 14% for a silicon triple junction cell (a-Si/nc-Si/nc-Si, stabilised) [51].

The working principle of a triple junction solar cell is based on the difference in band gaps of the sub cells. First, a top cell with a high band gap absorbs the short wavelength part of the spectrum. Ideally photons with an energy below the band gap energy are not absorbed, so the remaining part of the spectrum is transmitted. Next comes a middle cell with an intermediate band gap to absorb the middle part of the spectrum and a bottom cell with a low band gap to absorb the long wavelength part of the spectrum. By this approach, losses from non-absorption and thermalisation are reduced [52]. **Error! Reference source not found.** shows a schematic cell structure and the parts f the spectrum each cell utilises.

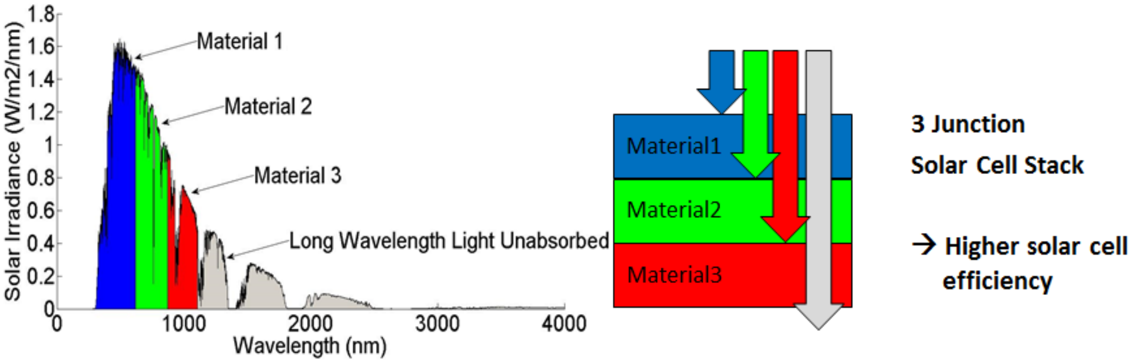

Figure 15: Light absorption in a triple junction solar cell, the spectral utilization (left) with the cell structure [53]

Mostly multijunction solar cells are monolithically deposited directly on top of each other, which can electrically be considered as a series connection of solar cells. For a series connection of solar cells, the voltage of all sub cells adds up to form the total voltage, and the current of the multi junction cell is limited by the lowest sub cell current. Since the charges need to travel from one sub cell to the next, recombination of charge carriers is needed at the junction between two sub cells, to from this series connection. This junction is therefore often called a Tunnel(ing) Recombination Junction (TRJ). For example, in a p-i-n/p-i-n junction, electrons from the top cell recombine with holes from the bottom cell, only electrons from the bottom cell and holes from the top cell are collected externally. This explains why the current density of a multi-junction solar cell is limited by the lowest sub cell current density, any additional charge carriers generated inside other sub cells cannot be collected [54].

The TRJ is an important factor to consider for a high quality multi-junction solar cell. A poor TRJ will reduce the V_{oc} and fill factor (FF) of a device, while increasing the series resistance [55]. The mechanism via which the recombination takes place is that the charge carriers tunnel to band tail defect states in the TRJ, after which they recombine [54], shown in Figure 16. It has been shown that several different approaches can enhance the TRJ performance, generally they deal with the addition of defect states within the TRJ. This can be done by adding an extra heavily doped layer [56], a microcrystalline layer [57] or an oxide layer. These extra defect states allow for better charge trapping within the band tail states in the TRJ, enhancing the desired recombination.

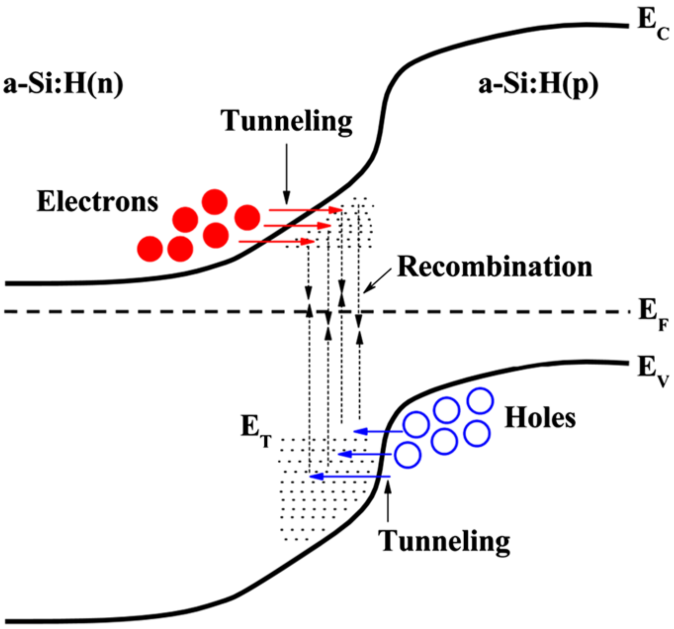

Figure 16: Tunnel Recombination Junction for a-Si [56].

2.4 Photoelectrochemical water splitting

In photoelectrochemical water splitting, the energy that is harvested by turning photon energy into electrical energy is used to drive the electrochemical reaction that splits water into oxygen and hydrogen. This section will take a short look at the electrochemistry of water splitting and explain different ways to produce hydrogen from sunlight.

2.4.1 Water splitting

Water splitting is the product of two half reactions involving water, oxygen and hydrogen. The exact nature of the half reactions depends on the acidity of the electrolyte. In an alkaline environment they can be written as follows:

$$4H_2O + 4e^- \leftrightarrow 2H_2 + 4OH^- \qquad E^0_{red} = -0.828\text{ V vs NHE} \qquad (5)$$

$$4OH^- + 4h^+ \leftrightarrow 2H_2O + O_2 \qquad E^0_{ox} = -0.401\text{ V vs NHE} \qquad (6)$$

In an acidic environment the half reactions do not contain the intermediate species OH^- but use H^+ instead, giving the following half reactions:

$$4H^+ + 4e^- \leftrightarrow 2H_2 \qquad E^0_{red} = +0.000\text{ V vs NHE} \qquad (7)$$

$$2H_2O + 4h^+ \leftrightarrow 4H^+ + O_2 \qquad E^0_{ox} = -1.229\text{ V vs NHE} \qquad (8)$$

The overall reaction can be obtained by adding 5 and 6 or 7 and 8. This overall reaction is the same for any (acidic or alkaline) environment, and H_2 is always formed at the cathode.

$$2H_2O \rightarrow 2H_2 + O_2 \qquad E^0_{redox} = -1.229\text{ V vs NHE} \qquad (9)$$

Reactions 5 and 7 are both called hydrogen evolution reaction (HER), and reactions 6 and 8 are called oxygen evolution reaction (OER). For any given redox reaction the Gibbs free energy change is given by the expression:

$$\Delta \mathrm{G} = -\mathrm{nFE} \tag{10}$$

where *ΔG* represents the Gibbs free energy change, *n* the number of electrons that are used each time the reaction takes place, *F* the Faraday constant (96485 C mol^{-1}) and *E* the total electrochemical potential of the reaction. At standard conditions, the electrochemical potential of -1.229 V gives a change in the Gibbs free energy of +237 kJ/mol H_2. This means that the reaction will not occur spontaneously, and 237 kJ of energy is needed to form on mole of H_2, but also it is the maximum possible energy that can be extracted from converting H_2 back into H_2O. This value of 237 kJ/mol H_2 however omits the excess heat input required due to the change in entropy during the reaction. The total chemical energy produced during this reaction is 286 kJ/mol, and to have thermoneutral electrolysis a potential of 1.48 V is needed [9]. It is possible to produce water below thermoneutral potential, but this will cool down the device. The theoretical efficiency at ideal reversible conditions with respect to the electrical energy can thus exceed 100%, because heat of the surroundings is incorporated into the reaction [58]. In real operation, this heat can often be provided by other losses in a system and in case of solar water splitting the sun's irradiation can provide extra heat needed [59].

Nevertheless, a device producing hydrogen will never operate at the equilibrium potential of 1.229 V, and significant overpotentials are needed for producing hydrogen at a relevant current density. The main source is the overpotential needed for the OER, although at increasing current densities the HER overpotential and voltage losses in the wires and electrolyte also start to play a role. As a result, the operational voltage for a device powering water splitting should exceed 1.6 V [60].

To evaluate the performance of PEC and PV electrolysis devices the ratio between the energy stored in hydrogen bonds and the incoming illumination energy is calculated. This often referred to as Solar-to-hydrogen (STH) efficiency, and is calculated as follows:

$$\eta_{STH} = \frac{J * E^0}{P_{in}} \tag{10}$$

where J represents the operating current of the device, E^o the equilibrium potential and P_{in} the incoming illumination power, in case of standard test conditions $1000 \mathrm{W/m}^2$. Note that this takes into account the electrical energy conversion and not the extra heat added due to the entropy change [61].

2.4.2 Solar water splitting technologies

It is possible to distinguish between technologies that use the electrolyte to form a semiconductor-liquid junction, which can be called a photoelectrochemical cell, and technologies that use solid state junctions wired to catalysts immersed in the electrolyte, commonly referred to as PV electrolysis. It is possible to take a mixed approach by having one semiconductor liquid junction which is biased with help of a solid PV junction. Many of the photocatalysts used in solar water splitting are metal oxides, due to their stability. However, many metal oxides suffer too much from poor charge carrier separation to absorb a sufficient amount of the solar spectrum [62]. A $BiVO_4$ photoelectrode coupled with an single junction a-Si cell was reported that reached a 3.6% STH efficiency by introducing graded doping in the $BiVO_4$ photoanode [63]. Other photocatalysts generally are thermodynamically unstable in water splitting conditions and tend to oxidize. Some p-type semiconductors however can be used in water splitting conditions, and an integrated monolithic PEC/PV cell using $GaInP_2$ for the photoelectrode and GaAs for the bottom cell was reported to show an STH efficiency of 12.4% [64].

Up till recently all devices with more than 10% Solar to Hydrogen (STH) efficiency use a form of solid junction with a double or triple junction solar cell, and most of them use III-V semiconductors [12]. It is expected that due to the expensive nature of III-V PV technology these technologies cannot be used to produce hydrogen in an economically viable way [65]. Recently a silicon heterojunction based design has reached a 14.2 % STH efficiency by using three series connected bifacial HIT cells to power a PEM electrolyzer [66]. This technology has the disadvantage of extra manufacturing steps needed to cut the HIT cells and connect the front side of the cell to the back side of the adjacent cell to form a series connection, but shows the promising possibilities of using PV electrolysis. Also devices using triple junction thin film silicon cells with STH efficiencies of more than 5% have been reported [12].

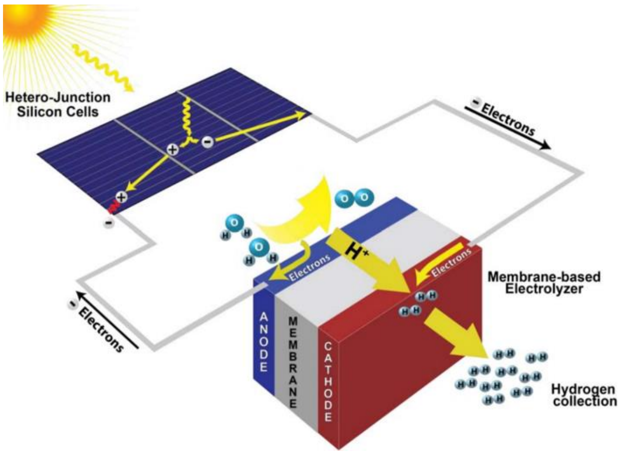

Figure 17: The PV electrolysis setup used to achieve 14.2% STH efficiency [66]

2.5 Research objective

To produce hydrogen efficiently with earth abundant materials, a silicon based triple junction solar cell is proposed in this work. This cell uses a silicon heterojunction, combined with nc-Si and a-Si thin film solar cells, to form a triple junction device. Combining these technologies gives the possibility to generate a high enough voltage and utilise a broad spectral range efficiently. Recently, such a device was made as part of a master thesis project in the PVMD group, the Netherlands, the structure is shown in Figure 18 [67]. This device showed a V_{oc} of 1.67 V and a J_{sc} of 8.5 mA/cm^2. When comparing the J-V curve with the counter electrode power curve a STH efficiency of 2.1% can be achieved, this is shown in the right part of Figure 18. Comparing this with the above described series connection of three HIT cells the performance is lacking. The V_{oc} for the triple junction device is much lower than the V_{oc} values of the three single junctions added together, and the fill factor is low, showing that the device has a high series resistance. Therefore, the research objective of this work is to improve the performance of this device by improving the V_{oc} and the current matching of the triple junction solar cell. This is done by investigating the possibility to improve several aspects of the design. Firstly, both tunnel recombination junctions can be a barrier for current transport and a source of recombination for charge carriers from one of the sub-cells. This causes the voltage of a triple junction device to be significantly lower than the voltage of the three single junctions combined. Furthermore, the thickness of the nc-Si middle cell (the current limiting cell) is increased to try to improve current matching of the device. Other points of interest are the interface between the top p-nc-SiO_x-layer and the TCO, and the TCO itself.

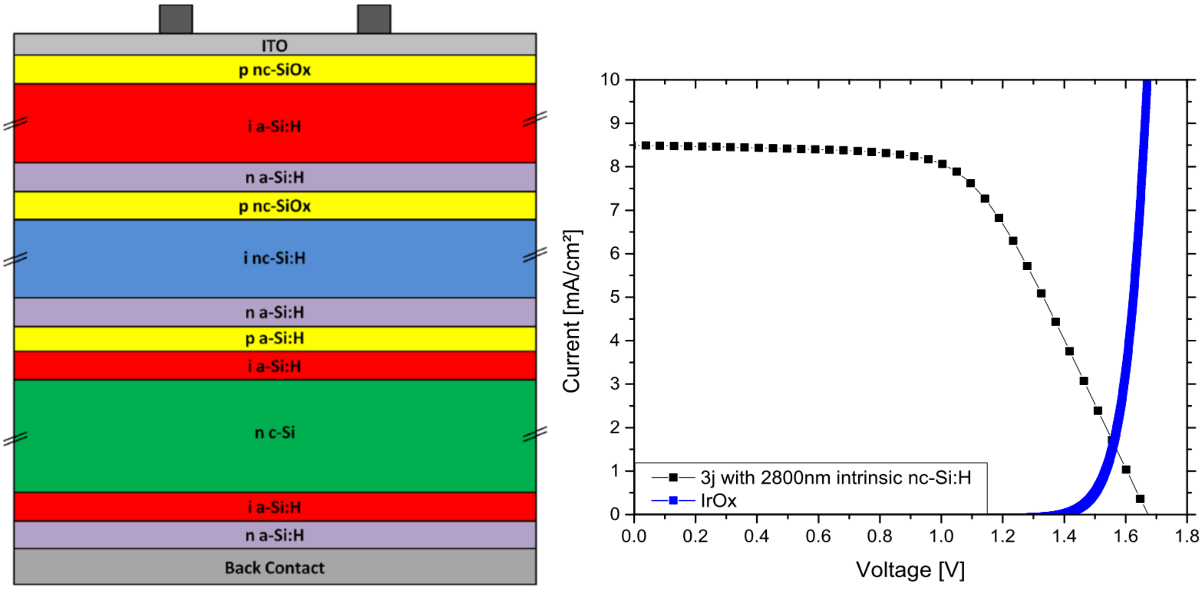

Figure 18: The triple junction solar cell design proposed in earlier work and the J-V curve of the triple junction solar cell, plotted together with the J-V curve of an IrO_x counter electrode.

3. Methodology

This chapter will introduce the techniques used for making and characterising the solar cells. The first section will describe the fabrication method for all samples, thereafter the measurement techniques for characterising solar cells will be explained.

3.1 Sample fabrication

Several different kinds of samples were made during this research. Next to the triple junction cells each sub-cell was fabricated as a single junction, and a-Si/nc-Si and nc-Si/c-Si tandem cells were made. For thin-film samples, flat corning glass was used as substrate, and the films were deposited by plasma-enhanced chemical vapour deposition (PECVD). Transparent conductive oxide (TCO) layers were deposited by sputtering, and metal front and back contacts were deposited by thermal and e-beam evaporation.

3.1.1 Substrate preparation

The c-Si wafers used are n-type <111> Float Zone (FZ) wafers (University wafer, 10-20 Ωcm). These wafers were cleaned by using the Nitric Acid Oxidation Cycle (NAOC). In this cleaning cycle, the wafers are first immerged for 10 minutes in 99.5% HNO_3 at room temperature to remove organic surface contamination and 10 minutes in 69% HNO_3 at 100°C to remove metallic surface contamination. These steps ensure the presence of an oxide layer at the surface, which is removed by a 2 minutes dip in 0.55% of HF [68]. Between each step the wafers are rinsed in demineralised water.

For the thin film single junction and tandem solar cells, flat corning glass was used as substrate. This glass was cleaned 15 minutes in acetone, followed by 15 minutes in isopropyl alcohol, both in an ultrasonic bath.

3.1.2 Plasma Enhanced Chemical Vapour Deposition

All silicon thin film layers used in this project are deposited with plasma enhanced chemical vapour deposition (PECVD). This is a deposition method to form thin solid films from vapour phase perquisites. Many different films can be created using PECVD, in this project PECVD is used for depositing amorphous silicon, nanocrystalline silicon and silicon oxide. The process starts by bringing a flow of reactant gas inside a vacuum chamber. In regular CVD, the gas phase reactants are activated by the high processing temperature. In PECVD, the gas phase reactants are activated by electron impact from a plasma, which is created by a RF alternating current. Reactants diffuse towards the substrate surface and absorb on the substrate surface to form a thin film. Positively charged ions created in the plasma will be accelerated towards the substrate surface [69].

The properties of the deposited film depend mostly on the reactive species, pressure, gas flow and RF power [70]. Because the substrate temperature has no direct influence on reactant activation, deposition can happen at relatively low temperatures. The film properties however can depend on surface temperature, as the surface temperature influences the mobility of atoms after deposition on the substrate [71].

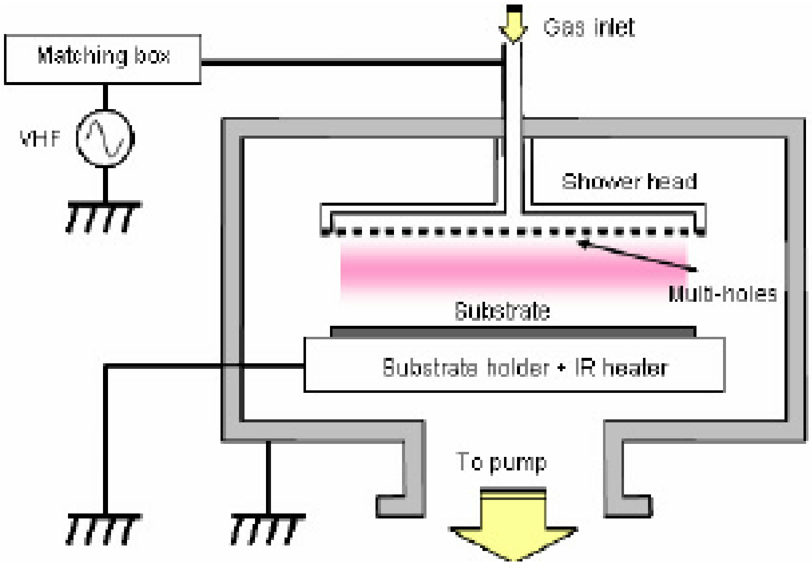

Figure 19: A schematic diagram of a VHF PECVD system for silicon(oxide) thin film deposition [72].

For processing the samples in this experiment two different PECVD machines were used, build by Elettrorava S.p.A from Italy. Figure 20 shows both machines, left is Amor, and right is Amigo. Both Amor and Amigo are multichamber systems with dedicated chambers for p- and n-type and intrinsic layers, to avoid contamination. After cleaning wafer substrates as described in section 3.1.1 they were transferred to Amor for the deposition of the a-Si layers that make up the HIT cell. Amor is equipped with a flipping stage to allow deposition on both side of the wafer without removing the wafer from vacuum, and thus avoiding the growth of any undesired oxide. After the i/n and i/p amorphous silicon layers were deposited the wafer is moved to Amigo where the p-i-n nanocrystalline middle cell and amorphous top cell are deposited. Samples without the c-Si bottom cell are processed only in Amigo. During the project, deposition parameters had to be adjusted due to chamber cleaning and or conditioning. Deposition times were calculated from test layers with the assumption of constant deposition rates with constant deposition parameters.

Figure 20: The PECVD equipment used, supplied by Elettrorava S.p.A.

3.1.3 Sputtering

A different technology for depositing thin films of material is Radio Frequency magnetron sputtering. This deposition technique can be categorised as a Physical Vapour Deposition (PVD) technique, meaning that the deposition gasses are supplied in a physical way. Just as with PECVD, it allows for low substrate temperatures. In PECVD the atoms for deposition are supplied in the gas phase. In sputtering a solid target is used, containing the material that is to be deposited. Between the target and the substrate an argon plasma is ignited. The ignition separates argon into Ar^+ and e^-. Due to the influence of an electric field (DC sputtering) or magnetic field (RF sputtering) the Ar^+ ions are accelerated towards the target, and the electrons are accelerated away from the target. The energy and momentum exchange upon collision of the argon ions with the target surface leads to a displacement cascade inside the target structure. Under influence of this displacement cascade, some of the target atoms will collide with enough energy and with the right direction to overcome the surface energy and be ejected, after which they can diffuse towards the substrate surface to be deposited there [72]. The electrons collide with other gas phase atoms to form new ions and sustain the plasma.

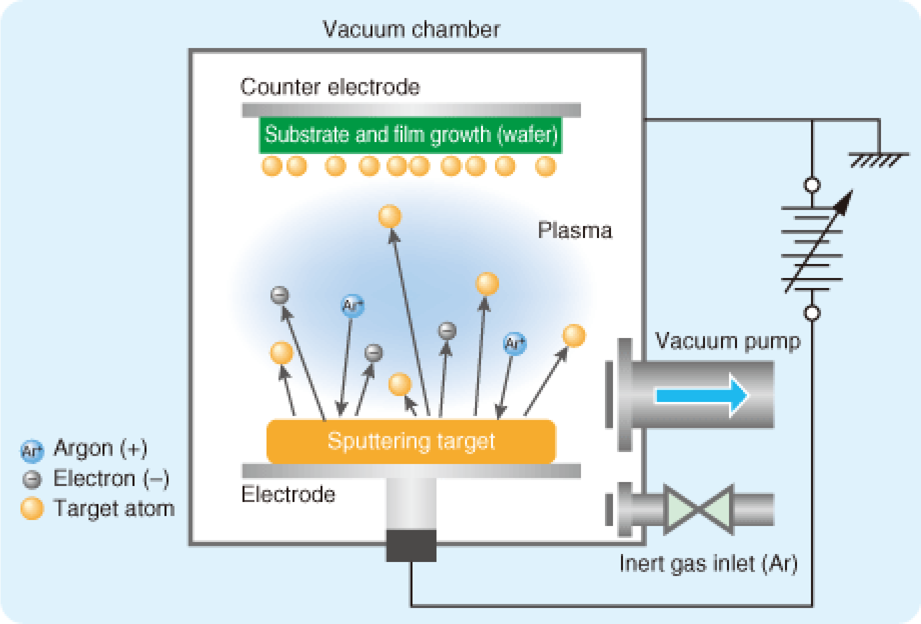

Figure 21: Schematic drawing of a RF sputtering system [73].

In this work aluminium doped zinc oxide (AZO) is used to form a back contact in case of samples deposited on glass substrates, and unless stated otherwise indium doped tin oxide (ITO) is used as a front TCO for all cells One experiment is done where hydrogenated indium oxide (IOH) is used as front TCO to make a comparison between ITO and IOH.

ITO deposition should be carefully fine-tuned, since the TCO should not only be transparent and have a high conductivity, but the deposition process should also avoid damage on the surface of the finished cells. The deposition is done directly on the p layer of the top solar cell (p-SiOx for the a-Si top cell), which limits the deposition conditions. High energy particles can have energies exceeding that of the Si-H bond (3.55 eV) and of a weak Si-Si bond (2.5 eV), producing the so-called ion bombardment. Therefore, they can affect the top layer, reducing the performance of the solar cell. Since the particle energy is directly related to the deposition power this power should be kept low, but high enough to sustain the plasma. Also, the temperature of ITO deposition should be considered carefully, since high temperatures will destroy the a-Si and nc-a-SiOx layers. On the other hand, low temperatures will cause the ITO layer to be less conductive [74]. In this project a temperature and power gradient for the ITO deposition is used to protect the solar cell structure from the higher deposition powers required for a good TCO layer. Deposition starts at 60 °C and 40 W. The temperature is gradually increased to 110 °C, and at 110 °C the deposition of the final ITO layer is done with 100 W for 2600 seconds, to create a layer with a thickness of approximately 100 nm. The IOH is deposited at room temperature with a power of 100 W, and annealed afterwards at a temperature of 175 °C, this gives a completely crystalline layer [75]. The AZO is deposited at 400 °C and 400 W for maximal conductivity, there are no underlying layers that can be damaged during the AZO deposition.

3.1.4 Thermal evaporation

Thermal evaporation was used to fabricate the solar cell front contact (500 nm Al on ITO) for all cells, a back contact on the AZO layer for thin film cells (500 nm Al on AZO) and a back contact and reflector for cells with the c-Si wafer (200 nm Ag/30 nm Cr/500 nm Al). This was done in a high vacuum PRO 500S metal evaporator by Provac. Silver was deposited by thermal evaporation. In this process current is sent through a resistive boat containing silver. This heats up the boat up to the melting point of silver, after which the metal starts to evaporate. The substrate is kept at room temperature, so silver vapour diffusing towards the substrate will condense and form a metallic layer. The pressure in the chamber should be low enough so that the mean free path is longer than the distance between evaporation boat and substrate [76]. Aluminium and chromium were deposited using electron beam evaporation. This works in a similar way as thermal evaporation, only the energy needed to vaporise the materials is supplied by directing an intense electron beam via electric and magnetic fields to strike the source material [77].

3.2 Measurement techniques

This section will present the measurement techniques used to characterise all samples. These are illuminated I-V, dark conductivity and External quantum Efficiency (EQE) measurements.

3.2.1 Dark I-V curves

Although solar cells operate under illumination, measuring their conductivity in the dark can be used to analyse them. In particular, measuring the conductivity of the Tunnel Recombination Junction (TRJ) can give an indication of the TRJ quality by calculating the activation energy (E_a). This can be done by measuring the I-V curve at different temperatures and using the Arrhenius relation:

$$\sigma_d(T) = \sigma_d e^{-E_a/kT} \tag{11}$$

where $\sigma_d(T)$ is the conductivity without illumination, σ_d is the conductivity prefactor, k is the Boltzmann constant and T the temperature in Kelvin. This measurement gives information about the TRJ quality, a lower activation energy means that the junction has good conductive and recombinative properties, required for a TRJ in multi junction solar cells [56].

3.2.2. I-V curves under illumination

The electrical behaviour of solar cells under illumination is one of the most important methods to characterise cells. Figure 22 shows an example of an I-V curve for a solar cell, with the corresponding P-V curve.

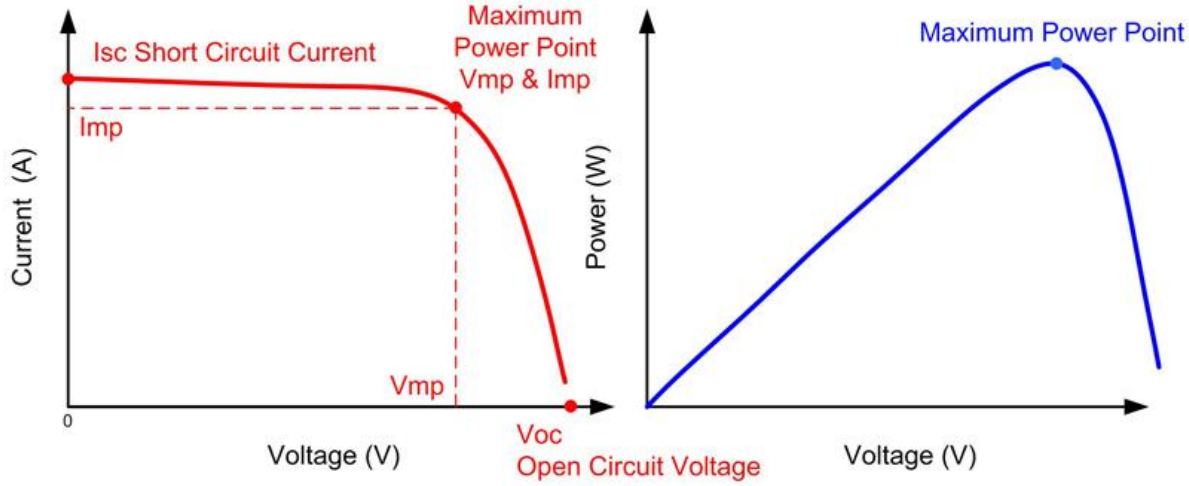

Figure 22: Typical I-V (left) and P-V (right) curve for solar cells [78].

There are several important parameters that can be taken from such a measurement.

- Short circuit current (I_{sc}): Current produced by the solar cell through an external short circuited circuit, so without load attached. Its dependency on the active solar cell area is often removed by dividing the current over the area to get the short circuit current density (J_{sc}). The short circuit current is directly related to the incoming illumination, as each absorbed photon generates one electron-hole pair.
- Open circuit voltage (V_{oc}): The voltage generated by the solar cell without external connection. It shows a small variation dependent on illumination according to:

  $$V_{oc} = \frac{nkT}{q}\ln(\frac{I_{sc}}{I_0} + 1) \quad (12)$$

  where n is the ideality factor, indicating how closely the solar cell approaches ideal diode behaviour, kT/q is the thermal voltage, I_{sc} is the short circuit current as described above and I_0 is the reverse saturation current. The reverse saturation is dependent on recombination inside the solar cell, and can vary with several orders of magnitude between solar cell devices with different quality. This is illustrated by the fact that high quality single crystalline solar cells can have V_{oc} values exceeding 700 mV, while commercial multicrystalline silicon solar cells typically have a V_{oc} of around 600 mV.
- Maximum power point (MPP): The operational point at which the solar cell produces maximum power. The current and voltage of this point are always lower than I_{sc} and V_{oc}.
- Fill factor (FF): The ratio between the maximum power generated by the solar cell and the product of short circuit current and open circuit voltage:

  $$FF = \frac{I_{mpp} * V_{mpp}}{I_{sc} * V_{oc}} \quad (13)$$

  This gives information about the losses inside the cell. If V_{mpp} is much lower than V_{oc} there is significant series resistance somewhere in the cell, increasing recombination. If I_{mpp} is much lower than I_{sc} the cells shunt resistance is not high enough, meaning that some of the current will find an internal circuit instead of going through the external load. These two situations are shown in Figure 23.

- Conversion efficiency (η): A percentage representing the ratio between the electrical power produced by the solar cell over the incident light.

$$\eta = \frac{I_{sc}*V_{OC}*FF}{A*P_{in}} = \frac{J_{mpp}*V_{mpp}}{P_{in}} \qquad (14)$$

where A is the solar cell area and P_{in} is the incident light power.

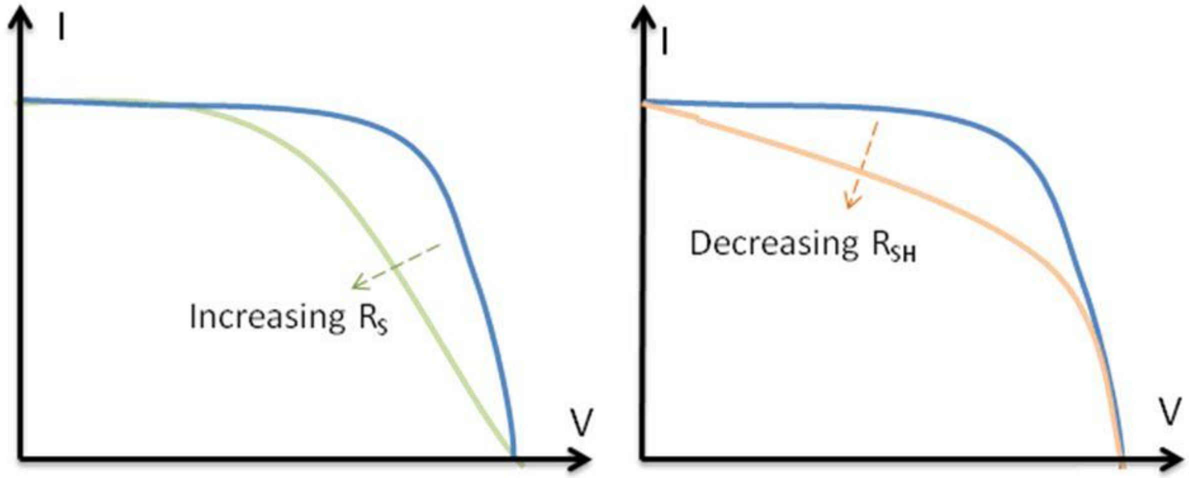

Figure 23: The effect of increasing series resistance (left) and decreasing shunt resistance (right) in a solar cell [79].

The measurements are carried out in a Wacom WXS-156S-L2 solar simulator. This simulator is equipped with a halogen and a xenon lamp to mimic the solar spectrum as closely as possible, and is a class AAA simulator [80]. Measurements are performed under standard test conditions (STC): 25°C and 1000 W/m^2 with an AM1.5 spectrum. The solar cells are mounted in their right holder and contacts are established with help of two probes. To prevent heating of the solar cell the measurement is done with a quick voltage sweep across the solar cell while measuring the current, and the stages are equipped with a cooling system.

3.2.3 External Quantum Efficiency

The external quantum efficiency (EQE) of a solar cell is the ratio of the collected charge carriers over the number of photons as a function of the wavelength of the photons (or the photon energy). If all incoming photons at a certain wavelength contribute to the current of a device, the EQE for that particular wavelength is one. Ideally the EQE for a solar cell is unity up until the band gap (below bandgap photons cannot contribute to the current), however, in each solar cell some loss mechanisms are present. Common losses are recombination at the front and back surface, reflection losses and other non-absorption losses. Figure 24 gives an indication of some of the losses.

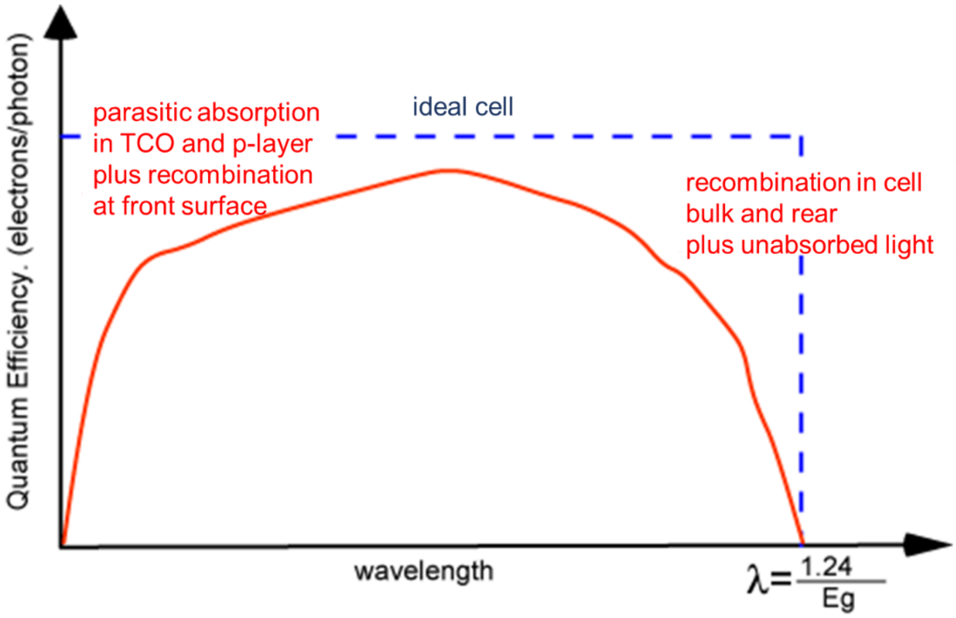

Figure 24: Typical EQE of an ideal (blue) and actual (red) solar cell, illustrating the impact of several loss mechanisms [81]

The EQE setup uses a xenon arc lamp light source in combination with a monochromator, a chopper and a lock-in-amplifier. Illumination with monochromatic light is necessary in order to measure accurately what the solar cells response is to photons of a particular wavelength. The chopper enables the setup to distinguish between the current produced by the light source and current produced due to other light sources. When the EQE curve of a solar cell is known it is possible to calculate the J_{sc} by integrating the product of the EQE at each wavelength and the AM 1.5 spectrum according to the following equation:

$$J_{sc} = -q * \int_{\lambda 1}^{\lambda 2} EQE(\lambda) * \Phi_{ph,\lambda}^{AM1.5} d\lambda \tag{15}$$

where *EQE(λ)* gives the external quantum efficiency and *Φ* the photon flux at each wavelength, and λ_1 and λ_2 represent the relevant boundary wavelengths. This J_{sc} value is used to correct the J_{sc} measured with the illuminated J-V curve in order to minimise the influence of spectral mismatch between the light source and AM 1.5. This is done according to the equation:

$$J(V) = J(V) * \frac{J_{sc,(EQE)}}{J_{sc,(J-V)}} \tag{16}$$

When measuring a multijunction solar cell there is a complicating factor. As explained before, in a multijunction cell each sub cell needs to contribute for current to be collected. If monochromatic light is incident on a triple junction solar cell no current will be generated, because the light is only absorbed in one sub cell (sometimes partially in two overlapping sub cells, but this is still an inaccurate measurement). The solution to this is using bias light to saturate two of the sub cells so that the EQE of the third sub cell can be measured. The measurement is then repeated with bias light of different wavelengths for each sub cell. When correcting the J_{sc} of a multijunction solar cell the J_{sc} of the sub cell with the lowest current is taken.

4. Results

This chapter will present and discuss the experimental results. In order to optimise the triple junction solar cell as proposed in the research objectives, a number of different cells were fabricated and characterised using the equipment and techniques explained in chapter three. First the experimental results of single junction cells will be presented, followed by the results of the micromorph and nc-Si/c-Si tandem cells and at last the results of the triple junction cells.

4.1 Single junction solar cells

The behaviour of solar cells in a single junction is not identical to their behaviour in a triple junction. However, some parameters can be optimised more easily in a single junction configuration because there are fewer variables that can influence cell performance. Also, when optimising some of the gas flows for the deposition recipe it is easier to do so for single junction cells.

The single junction crystalline silicon cell was made with the same layer structure as shown in Figure 14, except that the wafer is not textured in this work. Both the amorphous silicon and nanocrystalline silicon cells were deposited on flat glass. A layer of Aluminium doped Zinc Oxide (AZO) was used as a bottom conductive layer instead of the regular metal back contact. This was done to mimic the optical situation in the final triple junction cell, where light which is not absorbed after the first pass through the material will (mostly) not be reflected but absorbed in the layers below. The top TCO used was ITO, deposited on top of the p-a-Si layer. Aluminium contacts are used on top of the ITO, and Illumination is done through the top p-nc-SiO_x layer for the thin film cells and through the top p-a-Si layer for the c-Si cell. The thin film cells use aluminium contacts on the side of the AZO layer to establish a back contact, while the back reflector and contact for the c-Si cell consisted of thermally evaporated Ag/Cr/Al layers, deposited on the n-a-Si layer.

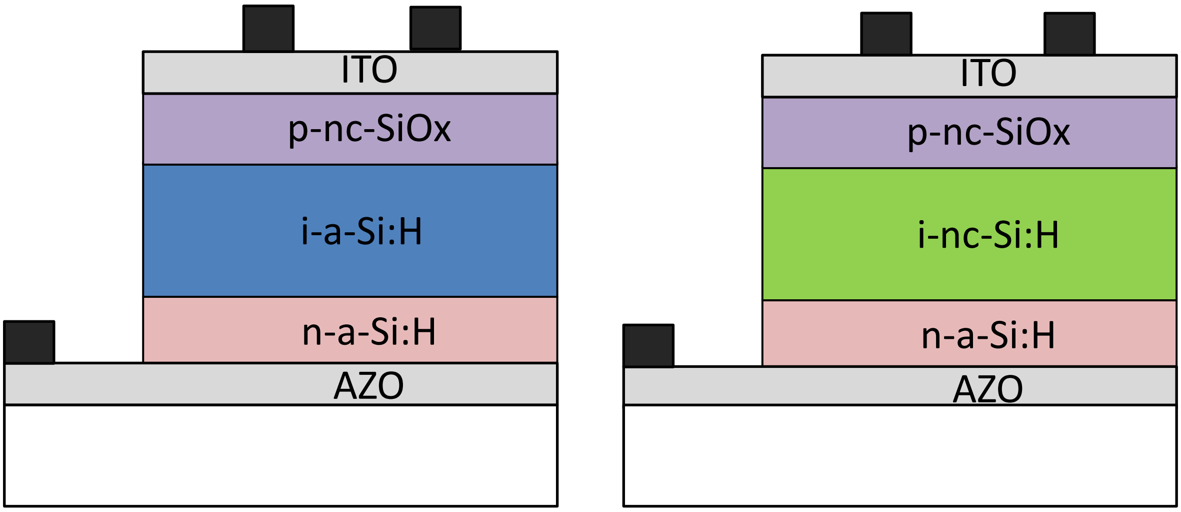

Figure 25: The structure of the a-Si and nc-Si cells made in this project.

4.1.1 Baseline single junction cells

Error! Reference source not found. shows the J-V curves for all single junction cells as a baseline or this project. When looking at the external parameters of the a-Si cell in Table 1, the first thing that can be noticed is that the FF and V_{oc} values for are rather low compared to literature values [82]. The presented a-Si cell only has a V_{oc} of 0.85 V and a fill factor of 0.55, while 0.9 V of V_{OC} and FF of 0.65 are achievable. A possible reason for the low electrical performance is that the interface between the front p-nc-SiO_x and the front ITO layer is forming a barrier for current transport. The J_{sc} is also quite low, but this is to be expected because there is no attention paid to light trapping yet. For the nc-Si cell the story is quite similar although the difference in J_{sc} is percentagewise smaller, so the efficiency does not suffer as much. Still, a V_{oc} of 0.45 and a fill factor of 0.59 are low compared to the record cells V_{oc} of 0.55 and FF of 0.73 [51]. This can be due to not only the TCO layer previously mentioned, but also to the difficulties that nc-Si encounters when growing on a flat surface, as would be explained later. In the case of the HIT cell, also the V_{oc} and fill factor are noticeably lower than values reported in literature, with FF of 0.64 and V_{oc} of 0.69 V, while these values can be as high as 0.8 for the FF and 0.74 V for the V_{OC} [51].

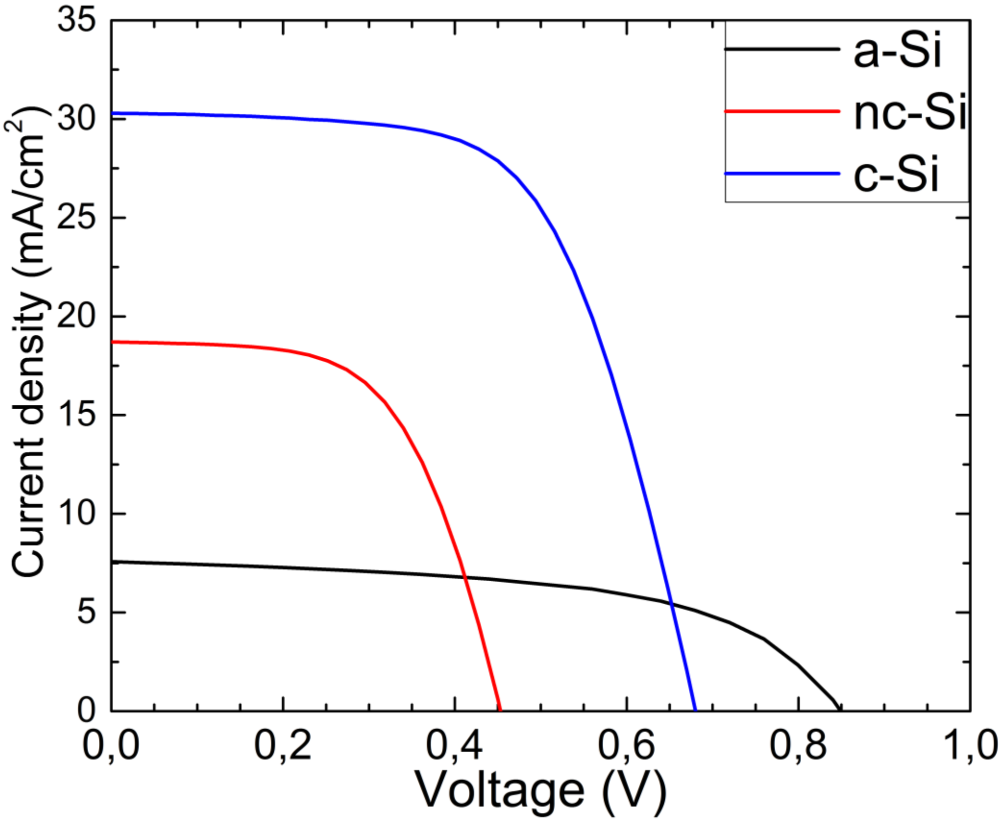

Figure 26: J-V curve for the baseline single junction solar cells.

Table 1: External parameters for the baseline single junction solar cells.

Sample	Voc (V)	Jsc (mA/cm^2)	η (%)	FF(-)
a-Si	0.85	7.6	3.3	0.55
nc-Si	0.45	18.7	4.9	0.59
c-Si	0.68	30.2	12.7	0.62

Apart from the fact that the deposition process for these cells was not fully optimised for single junction cells, an important reason for the low performance of the thin film cells might be the substrate used for deposition. The properties of thin film layers do not only depend on the process conditions, but also on the substrate itself. As example, a- Si layers deposited on glass/TCO/p-layer in general perform better than a-Si layers deposited on metal foil/TCO/p-layer [83]. Commonly a-Si and nc-Si cells are deposited in a p-i-n order [82], [84]. This allows the TCO on top of the p-window layer to be deposited first, giving more flexibility in choice of TCO material and deposition parameters. The TCO layer used in this project is less conductive, increasing the series resistances and thus lowering the fill factor. Apart from that does the order of deposition have an effect on the properties of the i-a-Si layer, and n-i-p cells commonly suffer from enhanced recombination compared to p-i-n cells due to dopant contamination [85]. This will lower the electrical performance of the cell.

Because the c-Si wafer will eventually form the substrate in this project, all cells were deposited in n-i-p configuration. This is done on top of an untreated layer of AZO which is directly deposited on a flat glass substrate. However, the untreated AZO layer is not flat, thicker layers of AZO will show a texture with v-shaped valleys [86]. The v-shaped valleys form a starting point for the formation of cracks in the material in the growth direction. These cracks form recombination centres which increase the J_0 and in turn decrease the V_{oc} of the device [87]. This principle applies both to a-Si and nc-Si cells [88], and could from a contribution to the low performance of the thin film solar cells presented here. Surface treatment can smooth the surface slightly and turn the valleys into u-shaped valleys, which reduces the formation of cracks [89].

4.1.2 Top p-layer for a-Si top cell

Other studies in this research group that hosted this project have focused on changes in the deposition parameters of the p-nc-SiO_x window layer of a superstrate p-i-n a-Si solar cell. They noticed that using a thin contact layer of p-a-Si (or p-nc-SiO_x with lower oxygen ratio) and using an extra step to passivate the dangling bonds of the i-a-Si/p-nc-SiO_x interface with hydrogen improves the performance of the total device by lowering the series resistance and increasing the shunt resistance, thus giving a better fill factor [82]. Although this project uses an n-i-p structure it is still worthwhile to test if these changes can improve the performance of the a-Si cell in this project.

Figure 27 shows the results for four different ways of depositing the top p-layer. It can be seen that only the sample in which both the extra hydrogen passivation and the p-a-Si contact layer are applied performs better than the baseline sample. The improvement mainly lies in a higher fill factor, as displayed in Table 2.

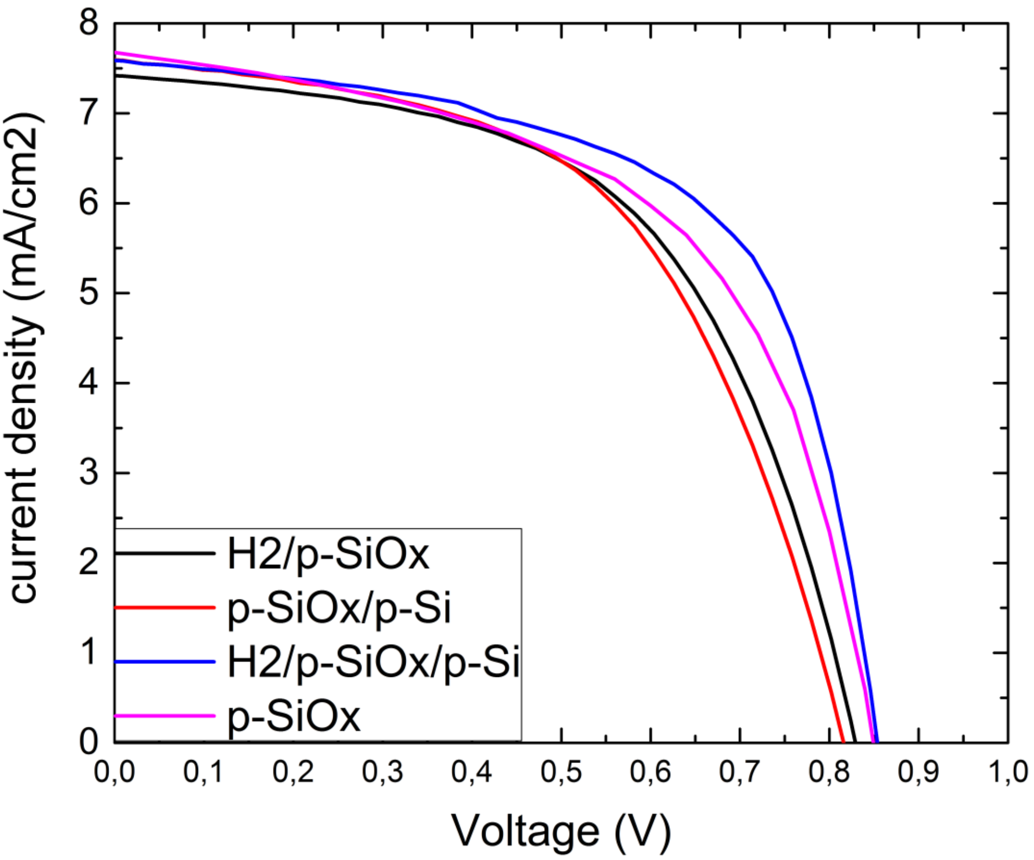

Figure 27: J-V curve for a-Si cells with a different top p-layer

Table 2: The V_{oc} FF, Rs and Rsh for the four a-Si cells

Sample	Voc (V)	FF(-)	Rs(Ωcm^2)	Rsh(Ωcm^2)
H_2/p-SiO_x	0.83	0.55	21.5	1077
p-SiO_x/p-Si	0.82	0.54	24.1	856
H_2/p-SiO_x/ p-Si	0.87	0.66	15.5	974
p-SiO_x	0.85	0.56	17.2	663

It is unclear why only using both of the suggested improvements increases the fill factor of the device. If both methods improve the current collection by improving charge transfer across the interfaces, one would expect each separate improvement to make a difference on its own. The hydrogenation step hydrogenates dangling bonds at the interface, thus reducing the surface recombination. By using a thin p-Si layer the resistivity can be lowered by forming a better contact between the ITO layer and the p-layer, while retaining the high selectivity of the p-SiO_x layer. The effect of these improvements can be seen in the H_2/p-SiO_x/p-Si layer.

Another interesting point to note is that J_{mp} for all four cells is considerably lower than J_{sc}, around 25-30% lower. This is a result of a too low shunt resistance. Together with the fact that these cells have a V_{oc} which is around 0.05-0.1 V lower than the cells from literature which are used as a comparison (section 4.1.1) this might indicate high density of cracks as described in section 4.1.1. This effect will probably be less present in the triple junction cells, and the improved a-Si cell recipe with an hydrogenation step and a thin p-a-Si contact layer will be used in the final triple junction cell design.

4.1.3 Absorber layer thickness for nc-Si middle cell

These cells were used as a starting point for further optimisation. The thickness of the absorber layers in the a-Si and nc-Si cell was 200 nm and 2800 nm respectively. Especially the a-Si layer is quite thin but since the layers have to be current matched eventually it was decided to start with a thin layer and increase the thicknesses were needed further on in the current matching process.

Simulations with GenPro4 have indicated that in the final triple junction device the nc-Si middle cell is likely to be the current limiting cell. The reason for this is that the a-Si absorption overlaps for a large part with the absorption of the nc-Si cell, while the nc-Si cells absorption towards the red side of the spectrum is limited. This is shown in Figure 28.

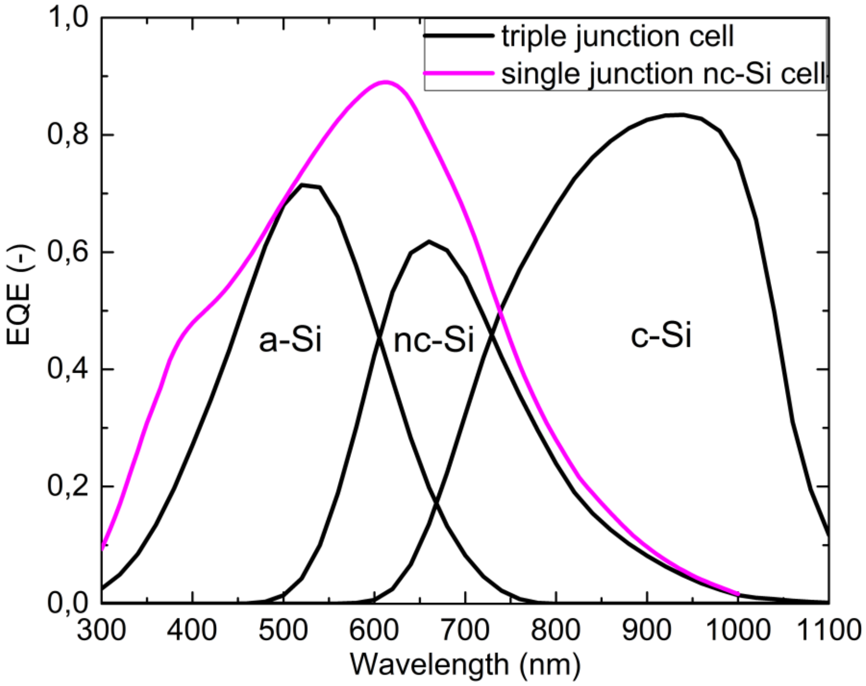

Figure 28: The simulated EQE for a triple junction cell and a single junction nc-Si cell

The same simulations indicate that making the nc-Si layer thicker would increase the absorption towards longer wavelengths, thus giving better current matching in the total device. Figure 29 shows the short circuit current density for all three sub cells as a function of the nc-Si cell thickness. All other layer thicknesses have been kept constant, except for the a-Si absorber layer thickness. It can be seen that the nc-Si layer thickness can be increased beyond 5 micrometres to improve the current matching of the total device. However, increasing the i-nc-Si layer thickness can also have a negative effect on the charge separation and collection. Thus, this balance has been studied further.

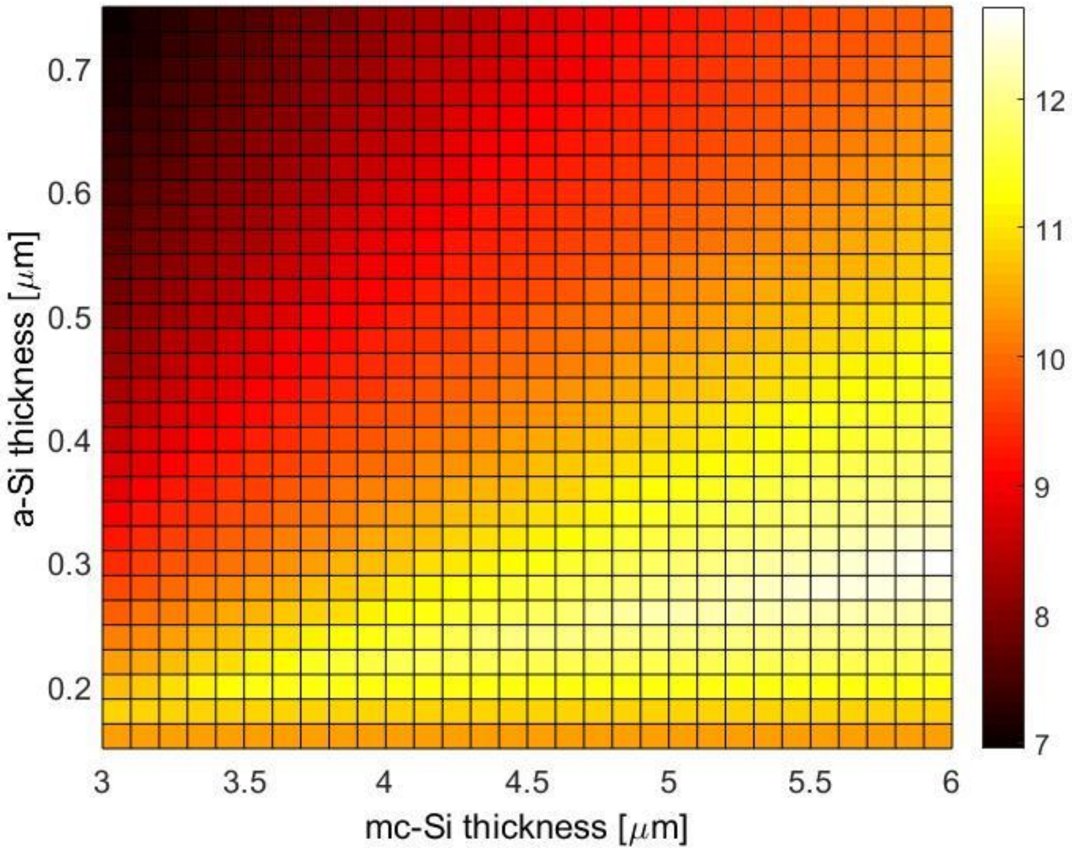

Figure 29: The simulated short circuit current density of all three sub cells for a triple junction solar cell as a function of the nc-Si cell thickness and the a-Si cell thickness.

Three single junction nc-Si cells were made to test these simulations. As can be seen from Figure 30 the absorption in the red wavelength region increases when increasing the absorber layer thickness. However, the relative difference between 3500 and 4000 nm is small. The high absorption difference in the blue region is likely to be caused by ITO irregularities. These measurements would suggest that using a thicker absorber layer is a good option to improve current matching. However, a thicker absorber layer commonly reduces the V_{oc} and FF of an nc-Si solar cell, since at some point the lifetime of the charge carriers would not be long enough to reach the contact [90], [91]. This would depend on the material quality.

Figure 31 shows that the cell with a 4000 nm absorber layer thickness shows reduced V_{oc} and especially FF compared with the 3500 nm thickness sample. The sample with a thickness of 3000 nm is clearly underperforming. Not only is the current relatively low (as that could also be explained by differences in the ITO layer) but the V_{oc} is also much lower than that of the other samples. **Error! eference source not found.** summarises the external parameters of the samples.

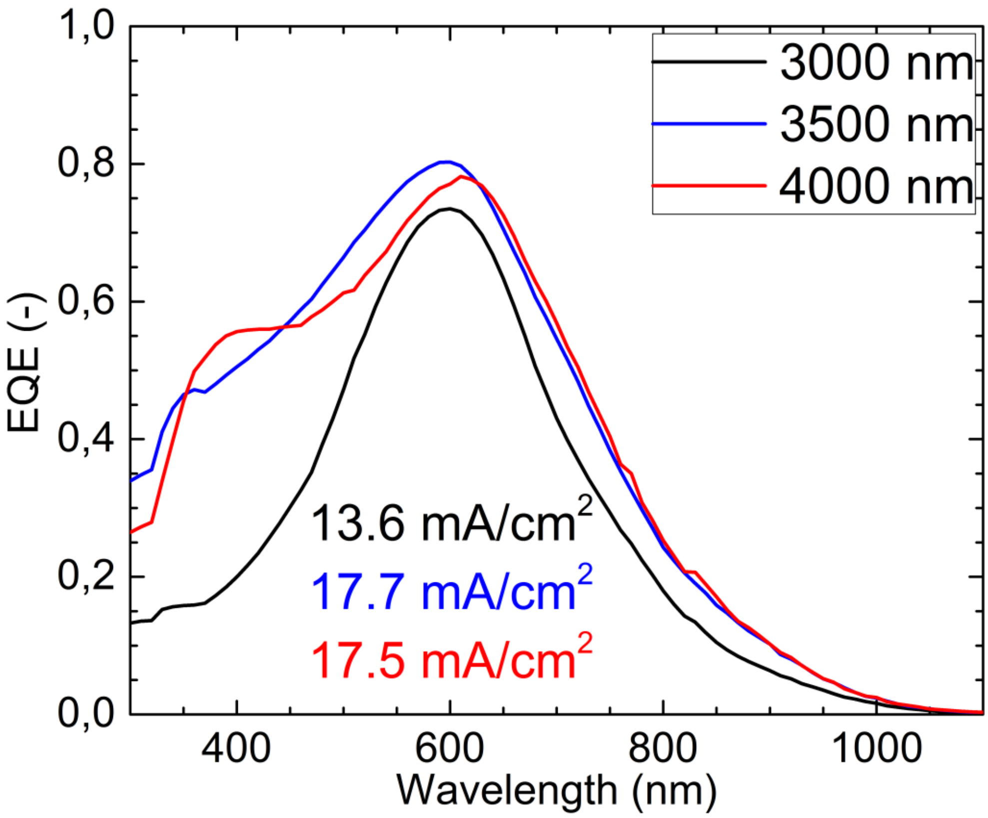

Figure 30: EQE curves for nc-Si cells with different absorber layer thickness

It is important to note that these samples were not co-deposited, but deposited one by one. Looking at both the EQE and J-V measurements, the sample with an absorber layer thickness of 3000 nm seems to have an internal defect that causes a lot of recombination. The V_{0c} is just 0.37 V, while the other samples reach 0.5 V. It is therefore difficult to make a comparison between using 3000 and 3500 nm absorber layer thickness in an nc-Si solar cell. A possible explanation of the low performance is related to the presence of shunt paths as explained in section 4.1.1. For thinner layers it is shown in literature that increasing the layer thickness decreases the formation of shunt paths inside the cell [92]. Thus, it could be that the thinner sample has more shunt path formation than the thicker samples and therefore has a lower performance. The fact that the performance is also worse than the first cell presented in section 4.1.1, with a thickness of 2800 nm, shows than that the formation of shunts is not a consistent process.

Also, when we compare the fill factor of the 3500 nm cell to that of the initial cell we can see that it is even higher than the initial nc-Si cells fill factor. Between these two experiments the deposition chambers of Amigo had undergone a cleaning procedure, after which the material properties were slightly varied. It is expected that this change has brought the nc-Si deposition recipe slightly closer to the transition towards the amorphous silicon deposition regime, resulting in an overall slightly better performance. Klein et al. [84] report an increase in both V_{oc} and FF when bringing the nc-Si deposition parameters increasingly closer to the transition towards a-Si. They also report that upon reaching this transition, a sudden loss in J_{sc} can be seen. The absorption in the long wavelength range decreases due to an increase in a-Si volume fraction, and the absorption in the short wavelength range decreases due to carrier extraction problems related to recombination. The 3000 nm absorber layer thickness shows comparable behaviour in the EQE measurement. The only difference is that for this sample also a drop in V_{oc} is observed, while that is not necessarily the case for cells deposited in the transition regime. Because of the positive result obtained with the 3500 sample all triple junction experiments were done with 3500 nm of nc-Si.

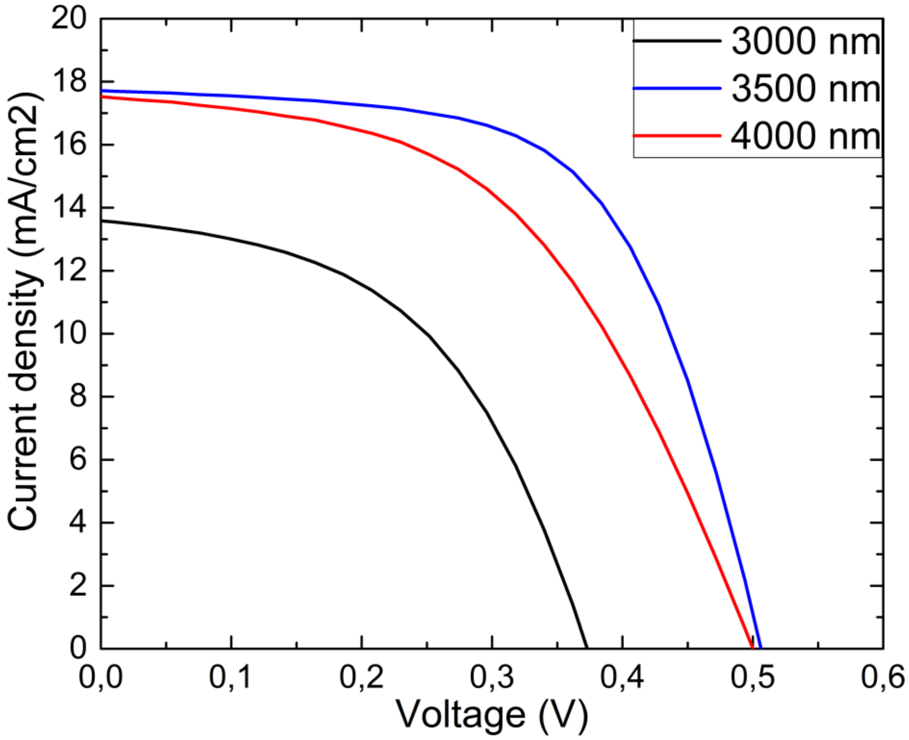

Figure 31: J-V curve for nc-Si cells with different absorber layer thickness

Table 3: External parameters for nc-Si cells with different absorber layer thickness

Sample	Voc (V)	Jsc (mA/cm^2)	η (%)	FF(-)
3000	0.37	13.6	2.5	0.49
3500	0.51	17.7	5.5	0.61
4000	0.5	17.5	4.4	0.5

4.1.4 Wafer passivation for HIT fabrication

In the previous project n-type <111> wafers from Topsil with a resistivity of 1-5 Ωcm were used. During this project these were not in supply, and wafers from University wafer, with a resistivity of 10-20 Ωcm are used. When comparing the J-V curve of these cells (black and pink in Figure 32) it can be seen that there is a decrease in electrical performance of the cells. For c-Si solar cells, the wafer edge is a potential recombination source. The HF dip in the cleaning procedure removes SiO_x and passivates surface dangling bonds with hydrogen. It could be that for the university wafer, more passivation is needed. Therefore the performance of solar cells with a duration of the HF dip of 60,90 and 120 seconds is tested, and compared to a benchmark solar cell from the Topsil wafer. The J-V curves are shown in Figure 32 and the V_{oc}, fill factor and shunt and sheet resistances are shown in Table 4. Figure 32 shows that with a cleaning time of less than 90 seconds the wafer is not passivated well enough, and the series resistance is higher than for the benchmark cell. However, with a cleaning time of 120 seconds the performance of the solar cell improved to even outperform the benchmark sample.

It is likely that using 120 seconds of HF dip removes some extra oxide that was not completely removed with a shorter dip, thus improving the passivation quality of the wafer. For the rest of the experiments, 120 seconds of HF dip is used for cleaning the wafers. It is possible that using a new batch of Topsil wafers and increasing the duration of the HF dip for those wafers would improve the performance of the HIT cell even more, because a lower wafer resistivity is expected to decrease the series resistance of the solar cell even further, thus increasing the performance.

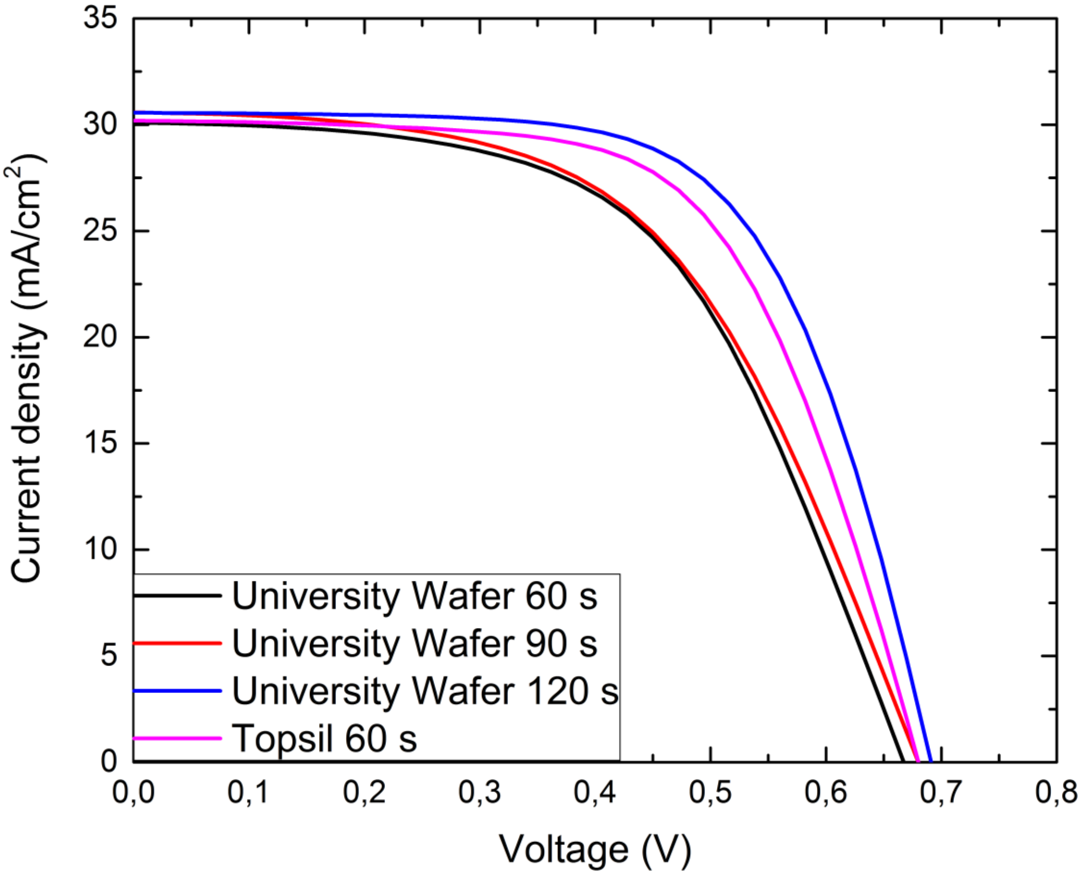

Figure 32: J-V curve for 4 HIT cells. One with a wafer from Topsil, and three from university wafer with different times for the HF dip in the cleaning cycle

Table 4: Electrical properties for the four different c-Si cells.

Sample	**Voc (V)**	**FF(-)**	**Rs(Ωcm^2)**	**Rsh(Ωcm^2)**
University 60 s	0.67	0.55	6.7	1531
University 90 s	0.68	0.54	6.1	1018
University 120 s	0.69	0.64	4.3	4702
Topsil 60 s	0.68	0.61	4.5	1428

4.2 Tandem solar cells

In order to determine the suitability of the Tunnel Recombination Junction (TRJ) strategies proposed, they were tested in tandem solar cells. In this section the results regarding the two tandem cell configurations are presented. For both the a-Si/nc-Si (micromorph) cells and the nc-Si/c-Si tandem cells the performance of the TRJ was tested. Also, for the a-Si/nc-Si TRJ, dark I-V curves and EQE measurements are made for samples with just the TRJ, without any intrinsic absorber layers.

4.2.1 a-Si/nc-Si

For this TRJ two types of experiments were done. Firstly, the performance of several isolated TRJ's deposited on Asahi UV were tested using EQE and dark IV measurements. These TRJs were then implemented into micromorph solar cells to test the performance under illumination. Three different TRJs were tested. For all junctions the p-layer was the p-SiOx layer as used for the nc-Si middle cell. For the n layer, it was chosen to see investigate the performance in case of using n-nc-SiOx, n-a-Si or an n-a-Si/n-nc-SiO$_{x.}$ Using I-V measurements the activation energy and dark conductivity for each layer were calculated.

Table 5: Activation energy and conductivity for three configurations of the top TRJ

Sample	Activation energy (meV)	Conductivity (S/cm)
n-nc-SiOx/n-a-Si	-2.99	0.123
n-nc-SiOx	30.1	0.00786
n-a-Si	91.65	0.0065

Table 5 shows the activation energy and conductivity of these samples. Sample 1 has a negative activation energy. With an increase in temperature, the conductivity goes down, instead of going up for the other two samples. A negative activation energy on itself has no meaning in the Arrhenius relation. However, one can explain this apparent negative activation energy in terms of a two-step process in which both steps have a positive activation energy [93]. The first step of such a process is a reversible equilibrium step, and the second step is irreversible:

$$A \rightleftharpoons B \rightarrow C \qquad (17)$$

If an increase in temperature increases the rate of B→C more than B→A the overall activation energy as determined by the Arrhenius relation can become negative. This happens if the forward reaction is entropically not favoured, if there are less microstates of the system which would lead to C compared to those that would lead to A [94]. It is speculated that this behaviour arises from the Si/SiO$_x$ configuration in the n-layer, current transport from the n-a-Si layer to the n-SiO$_x$ layer would in that case be a reversible process. On the other hand, the tunnelling of electrons from the n-SiO$_x$ layer to the band tail states, where they recombine with holes from the p-SiO$_x$ layer, would be an irreversible process. This is in accordance with the observation that electron capture in the tail states is the rate limiting step for current transport across a TRJ [56]. The conductivity of the n-nc-SiO$_x$/n-a-Si sample is considerably higher than of the other samples. These measurements suggest that using the combined nc-SiO$_x$/a-Si configuration for the p layer the barrier for charge transport across the TRJ can be reduced significantly.

These different TRJ's were applied to micromorph solar cells in order to confirm the performance in solar cell operation. Figure 33 shows the J-V curves of these solar cells. All solar cells have a high series resistance, probably related to problems with the TCO. However, the sample with 6 nm SiO$_x$/20 nm a-Si shows the highest fill factor, and does not have charge transport barrier as can be seen with the other samples. The samples with only SiO$_x$ show the lowest current and efficiency. All samples have an extremely high series resistance. While writing this thesis it was discovered that the sample heater inside the ITO deposition chamber was broken, which means that the deposited ITO has a much higher series resistance than normal. This makes it more difficult to compare the electrical behaviour of the samples. The differences in fill factor however can still suggest the improvements related to a certain configuration.

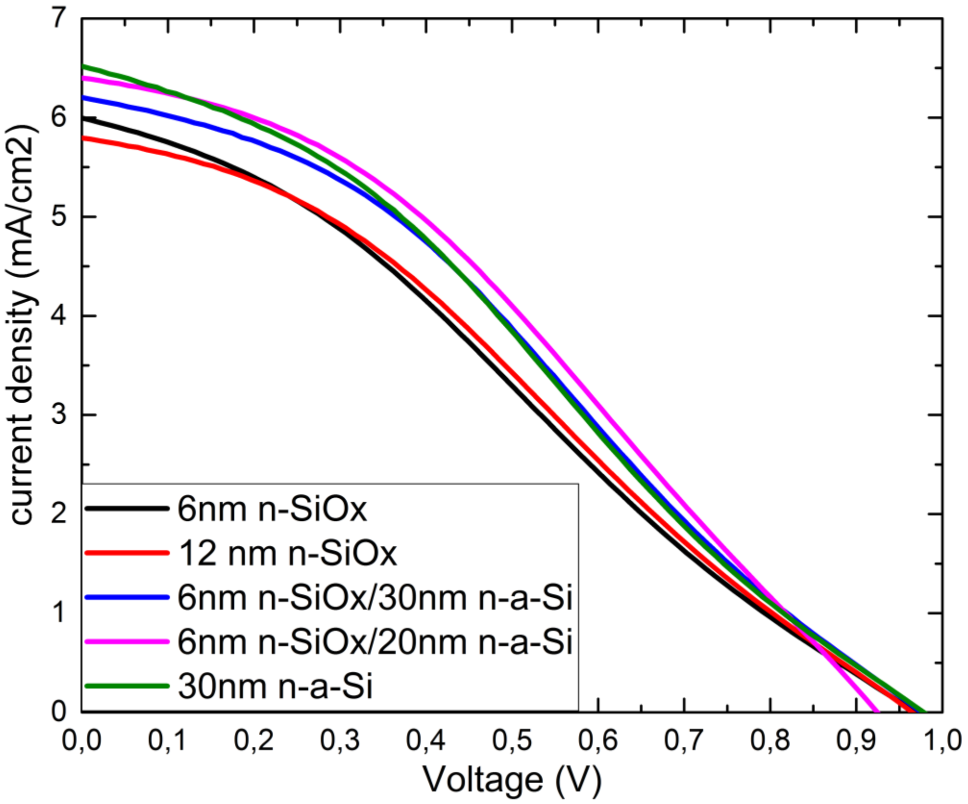

Figure 33: J-V curves for micromorph solar cells with different n-layers in the TRJ

Table 6: External parameters for micromorph cells with different n-layers in the TRJ

Sample	Voc (V)	Jsc (mA/cm^2)	η (%)	FF(-)
6 nm SiO$_x$	0.97	6.0	1.69	0.29
12 nm SiO$_x$	0.96	5.8	1.74	0.33
6 nm SiO$_x$/30 nm a-Si	0.97	6.2	1.9	0.32
6 nm SiO$_x$/20 nm a-Si	0.94	6.4	2.1	0.35
30 nm a-Si	0.97	6.5	2.0	0.31

Figure 34 shows the EQE measurements for all samples. These measurements show a higher absorption in the nc-Si cell for samples with an n-a-Si layer. The increase is not related to reduced absorption in the a-Si cell, since the thickness of the intrinsic top layer remains the same, and since for sample 3 and 4 only an extra layer of n-a-Si is added it can also not be related to parasitic absorption. This means that the overall current collection of the nc-Si cell increases when using a-Si compared to using SiO$_x$ for the n layer. The sample with 12 nm of SiO$_x$ shows the highest absorption in the a-Si cell and the lowest absorption in the nc-Si cell. Due to its lower refractive index, SiO$_x$ can be acting as an intermediate reflective layer [95]. The same effect however is not seen for the sample(s) with 6 nm of n-SiO$_x$. Probably 6 nm of SiO$_x$ is not enough to form an effective intermediate reflective layer.

For the triple junction cell, this reflective effect in the junction between the top and middle cell is not desirable. The nc-Si cell is current limiting in this device, and the reflective layer only decreases the amount of light available for the nc-Si cell. Using n-a-Si on the other hand increases the current in the middle cell, and is therefore a good choice. Electrically, the performance of the sample with 6 nm n-SiO$_x$/20 nm n-a-Si is best, and that configuration will later be implemented in the triple junction cell.

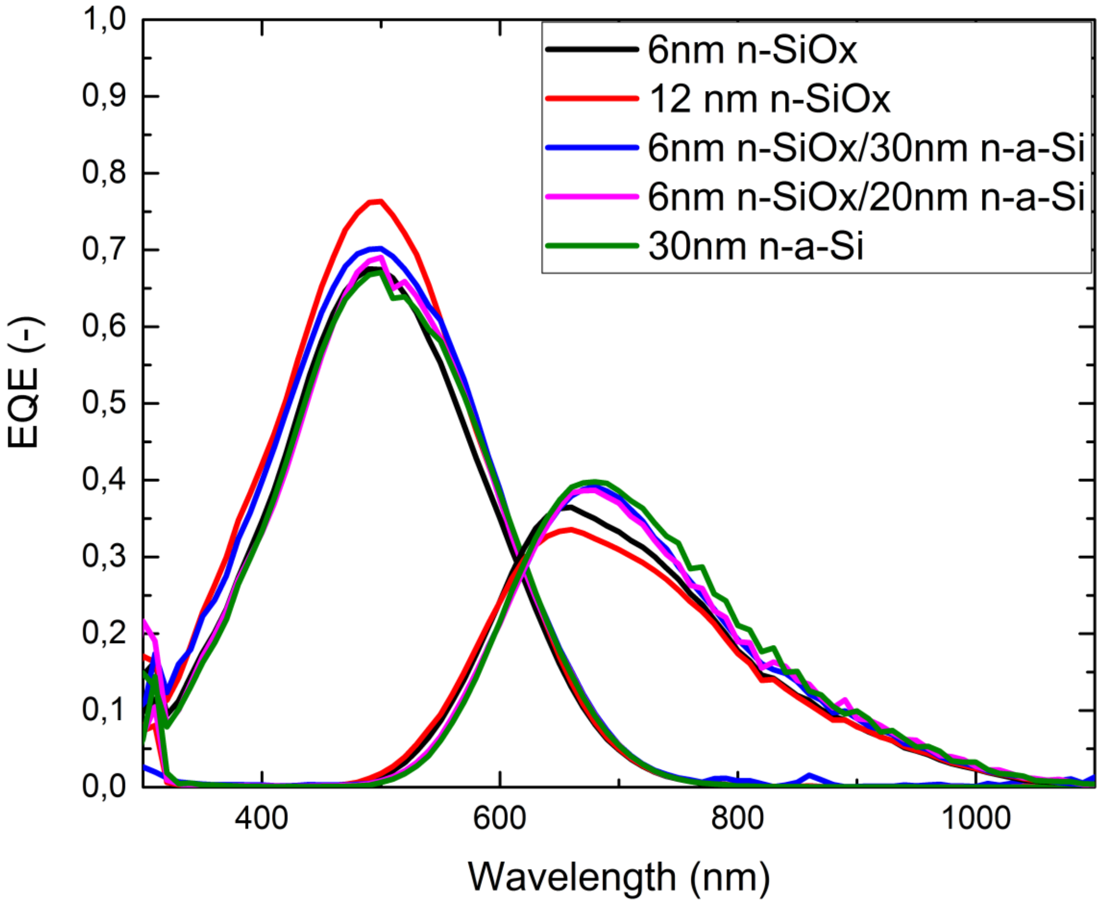

Figure 34: EQE measurements for micromorph solar cells with different TRJ configurations

Table 7: J_{sc} values for both sub cells of the tandem junction a-Si/nc-Si cells

Sample	**Jsc a-Si (mA/cm^2)**	**Jsc nc-Si (mA/cm^2)**
6 nm SiO_x	8.1	6.0
12 nm SiO_x	9.4	5.8
6 nm SiO_x/30 nm a-Si	8.8	6.2
6 nm SiO_x/20 nm a-Si	8.4	6.4
30 nm a-Si	8.4	6.5

4.2.2 nc-Si/c-Si

Lee et al. [56] have shown that for tandem a-Si/c-Si cells, improving the dopant concentration in the n layer of the TRJ leads to an improvement in the cells performance. A higher doping level leads to an increase in band tail defect states which enhances hole capture from the valence band. As a result, the barrier for recombination is reduced, so there is less accumulation of charge carriers and the cell's V_{oc} and FF improve. To test this performance increase of the TRJ for an nc-Si/c-Si tandem junction, several solar cells were made with different dopant gas flows during deposition of the n-layer from the top nc-Si cell. Figure 35 shows that both the 14 and 17 sccm sample show an improvement in series resistance and FF compared to the baseline sample. The S shape in the curve of the 11 sccm sample close to the x-axis is less prominent in both other samples, which is also reflected in the FF. This indicates that the 11 sccm sample has a barrier for charge transport which is reduced (but not completely removed) in the other samples. Also, the current and the V_{oc} of the sample with 14 sccm is considerably higher than the current of the other two samples. This could be caused by a better balance between internal recombination and charge transfer.

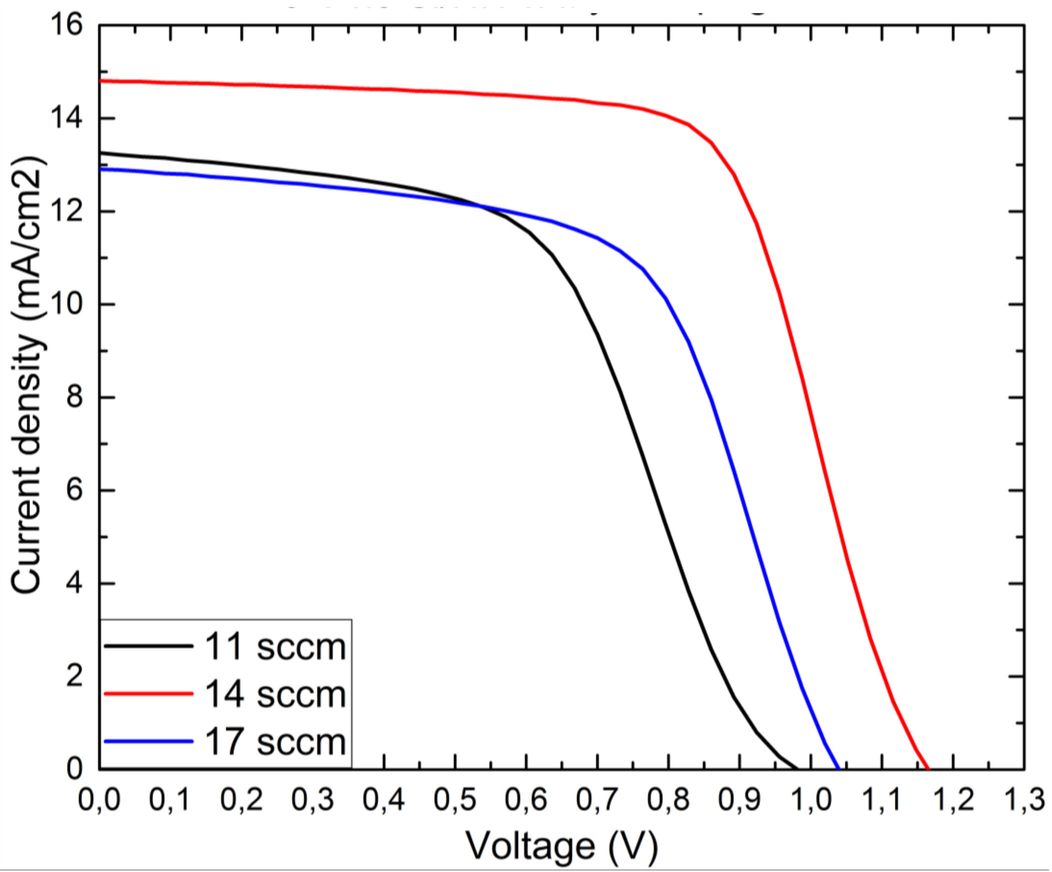

Figure 35: J-V curves for samples with different gas flows during n-a-Si deposition

Table 8: External parameters for three tandem junction nc-Si/c-Si cells with different dopant gas flows during deposition of the n-layer of the TRJ

Sample	Voc (V)	Jsc (mA/cm^2)	η (%)	FF(-)
11 sccm	0.98	13.2	7.1	0.54
14 sccm	1.17	14.8	11.5	0.67
17 sccm	1.04	12.9	8.2	0.61

Figure 36**Error! Reference source not found.** shows that the increase in current for the 14 sccm sample is mainly due to extra absorption in the short wavelength region of the spectrum. The difference in EQE at the blue part of the spectrum is also seen in single junction nc-Si solar cells that were co-deposited with the nc-Si top cell for the tandem cells. Combined with the fact that short wavelength photons will be absorbed closer to the p-SiO$_x$/i-a-Si interface, the difference in absorption will probably be due to a variation in that interface or the ITO/p-SiO$_x$. In the 600-900 nm wavelength region both 14 and 17 sccm samples have a slightly higher absorption in the nc-Si sub cell. Since short wavelength photons will be absorbed closer to the top of the absorber layer and long wavelength photons throughout the whole absorber layer the latter difference is more likely to be caused by an increase in TRJ performance. The EQE of the HIT sub-cell shows a slight increase too, which is another indication that the TRJ is improving charge carrier separation and collection. Since there is no TRJ related difference in current collection between the 14 and 17 sccm samples, and the 14 sccm sample has the best electrical performance, 14 sccm dopant gas flow is used for the triple junction cell.

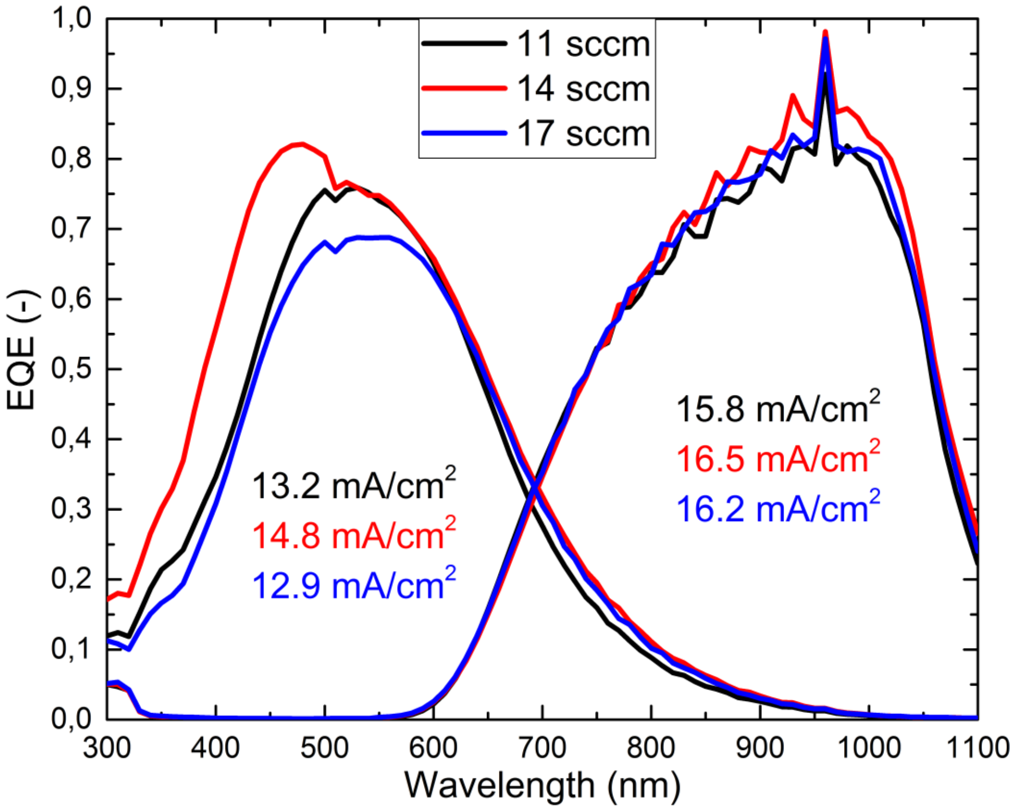

Figure 36: EQE for both the nc-Si and c-Si sub cells for three samples with different dopant gas flows

One problem arose during this experiment and all subsequent experiments where an nc-Si layer is deposited onto the flat wafer that was used as the bottom c-Si cell and substrate. Parts of the nc-Si layer did not stick to the wafer after deposition and fell off. This resulted in a damaged and shunted nc-Si layer. Figure 37 shows the damage to the cell. The measurements shown here are all from cells where this damage was not present, cells with the damage behaved as low performance c-Si single junction cells. Darker spots are parts were the nc-Si layer did not attach to the wafer. The right side of the sample has some working cells, without apparent damage. However, further damage invisible to the naked eye cannot be confirmed, and could explain some of the inconsistencies seen in these cells.

It is speculated that the nc-Si layer does not attach properly to completely flat surfaces, and that the partial attachment is due to the inherent roughness of the p-a-Si and n-a-Si layers of the TRJ. It must be noted that with higher doping gas flows the fraction of damaged area increases. It could be that higher doping levels make it harder to form a stable n-a-Si/i-nc-Si interface, or that a higher dopant gas flow decreases the as-deposited roughness of the n-a-Si layer. A possible way to mitigate this is by using a graded layer, so that the doping level is higher in the TRJ for good recombination and lower at the nc-Si interface to give a better nc-Si deposition.

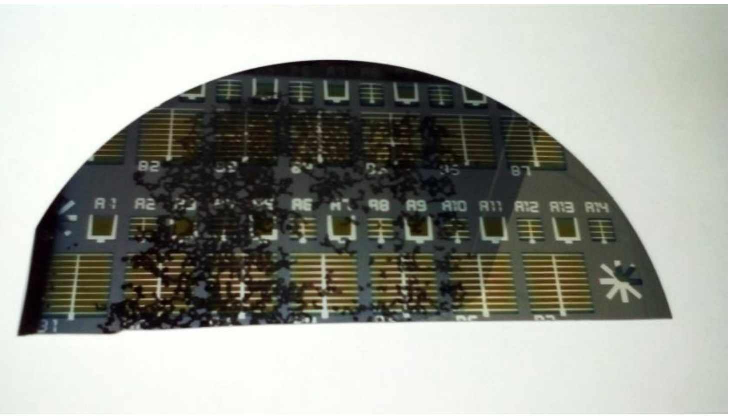

Figure 37: Damage to the nc-Si layer (darker spots) is visible on the cell

4.3 Triple junction cells

The previously described experiments indicated design improvements that can be implemented in a triple junction solar cell. These changes were all put together into an improved recipe for the triple junction solar cell. This new recipe is used for two experiments. First, the new recipe is compared to the original one, as was proposed in the previous master thesis [67]. After that, a comparison will be made between ITO and IOH as front TCO. This was done because it was expected that the ITO layer was not performing well as a front TCO, and IOH is known to be a suitable and good working front TCO.

Figure 38 shows the J-V curve for two samples. The initial one was done following the recipe of Falkenberg [67], while the final one integrated all the advances previously discussed. It should be noted that the initial sample has an a-Si layer thickness of 225 nm, while the final sample has a thickness of 200 nm. It is expected that this small change has not much influence on the cell performance. The absorption in the top a-Si cell will be a bit lower, leaving more light for the middle nc-Si cell. The higher overall J_{sc} for the final sample can in part be attributed to this fact. Apart from this it can be seen that the performance of the final sample is much better than that of the initial sample. The main difference is in the fill factor, due to a lower series resistance. The black graph also indicates there is a barrier for current transport by the slight S-curve behaviour. This could both be a barrier by less efficient TRJ's or a transport barrier across the p-SiO_x/ITO interface at the top of the cell. It cannot be exactly indicated which of the applied changes has the largest effect on the cells behaviour. However if we look at the relative difference made by each experiment in section 4.1 and 4.2, it is most likely that the improvement of both TRJ's is having the biggest influence on the performance. It should be noted that the problem with ITO deposition as described in section 4.2.2 was also present during the deposition of these samples. The overall effect is lower due to the higher V_{oc} of this device, but one would expect the performance to be better with the intended ITO layer.

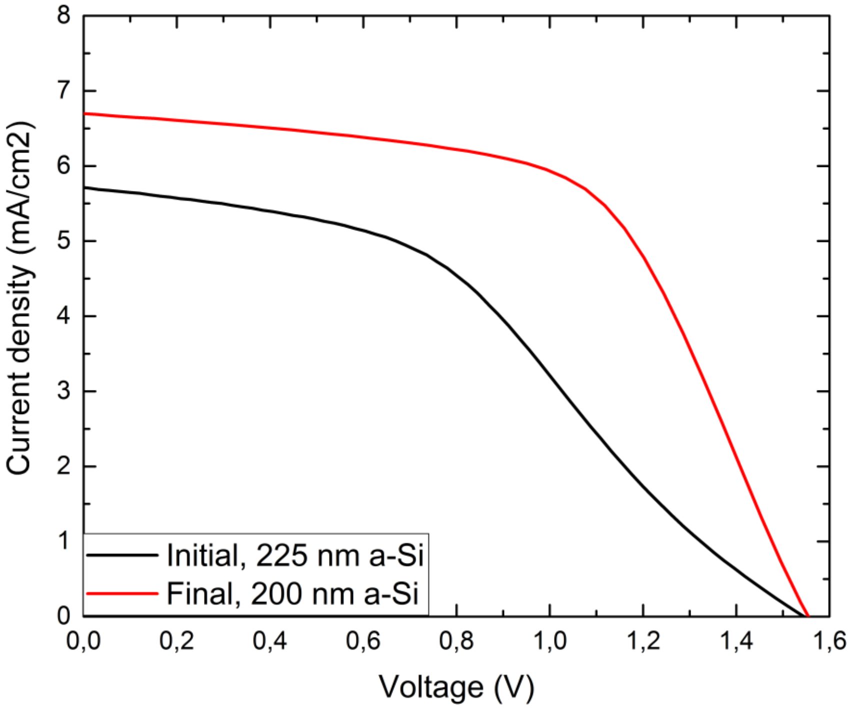

Figure 38: J-V curves with initial layer deposition parameters (black) and final deposition parameters (red).

Table 9: The external parameters for both triple junction cells

Sample	Voc (V)	Jsc (mA/cm^2)	η (%)	FF(-)	Rs(Ωcm^2)	Rsh(Ωcm^2)
Initial	1.54	5.7	3.6	0.42	266	1685
Final	1.55	6.7	6.2	0.59	103	2929

Figure 39 shows the EQE of each sub cell for the triple junction cell. It can be seen that the absorption is increased throughout the complete relevant wavelength range, which is an indication that charge separation and collection improved throughout the whole device. The EQE shows that the currents for each sub cell are not matched, with the nc-Si middle cell being limiting. The two main causes of this effect are the low absorption in the nc-Si sub cell and the low overall absorption in the middle wavelength region. Moreover, no texturing is used to improve the optical path length of light throughout the material. As a result, light only passes once in a straight path through each cell before hitting the back reflector. At that point all shorter wavelength light has been absorbed by the c-Si layer, and with the low absorption coefficient of nc-Si the overall absorption in that layer is low.

Moreover, the graded ITO layer used in this project has an increase in reflection in the 500-700 nm wavelength region. This limits the number of photons available for the nc-Si middle cell. It can be noticed that the absorption of the a-Si cell is noticeably higher at the lower wavelength sides. The higher energy photons are mostly absorbed close to the p-nc-SiO$_x$/i-a-Si interface. This might be the effect of better interface passivation, as explained in section 4.2.1, which more than compensates for the 25 nm thinner absorber layer. The absorption increase in the nc-Si cell is relatively the highest. This sub-cell is sandwiched between both TRJ's, and improving the electrical properties of the TRJ's will have a big impact on performance of the nc-Si cell.

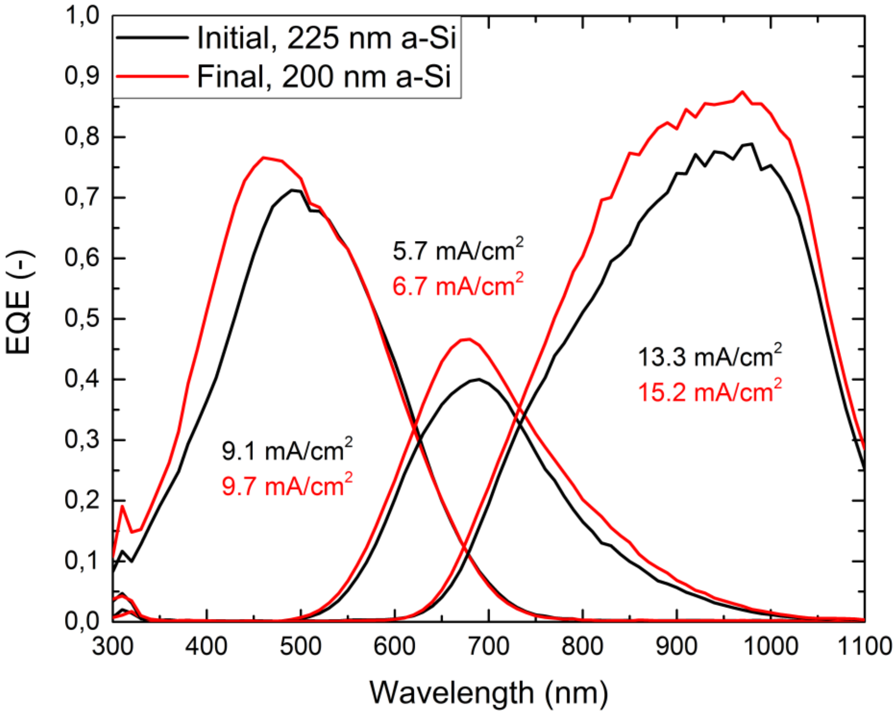

Figure 39: EQE measurement for each sub cell of the two different triple junction cells.

Because of the problems with the ITO top layer used, triple junction cells with hydrogenated indium oxide (IOH) as a front TCO were made. Also, IOH is known to be more conductive and transparent than ITO. Figure 40 shows a comparison between the EQE of the two identical triple junction cells, one with approximately 100 nm of ITO and the other with 80 nm of IOH as transparent conductive layer. It can be seen that the absorption in the middle wavelength region is much higher for the cell with an IOH top layer compared to the cell with an ITO top layer. A small decrease between 400 and 500 nm can be seen, but because the a-Si sub cell is not the current limiting cell this has no influence on the total current. It is possible that a comparable effect could be achieved by using a thinner ITO layer, but this would reduce the lateral conductivity of the layer.

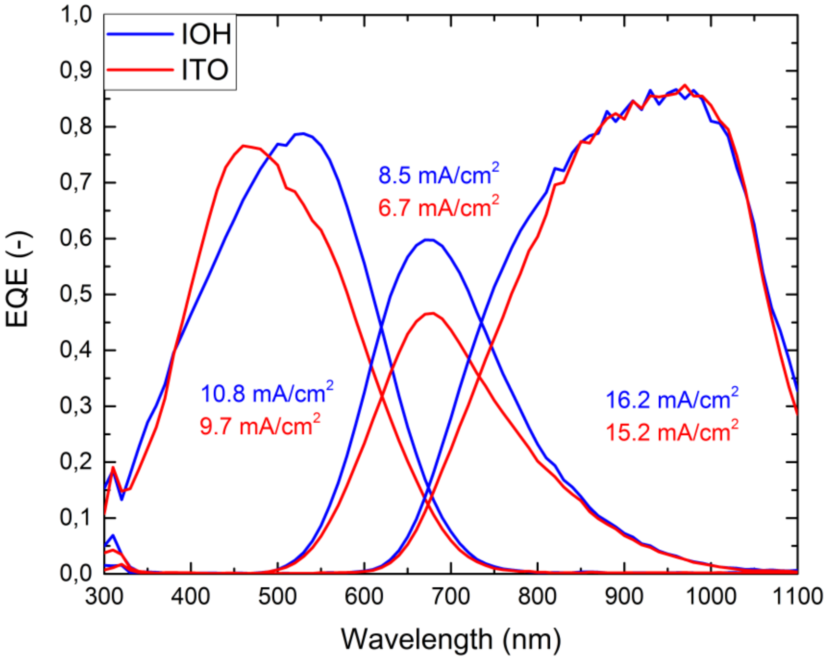

Figure 40: EQE measurement for a triple junction cell with IOH (black) or ITO (red) as TCO

Figure 41 shows the reflectance of both the ITO and the IOH layers. It is clear that ITO has a higher reflectance in the 550-750 nm wavelength region, which is where the nc-Si cell absorbs most of the light. Although IOH has a slightly higher reflection at the low and high wavelength ends, its optical performance for this triple junction cell is much better than that of ITO. It is expected that using a thinner ITO layer would shift the reflectance peak to lower wavelengths, but this would reduce the conductivity of the layer, and thus increase the series resistance of the cell even further.

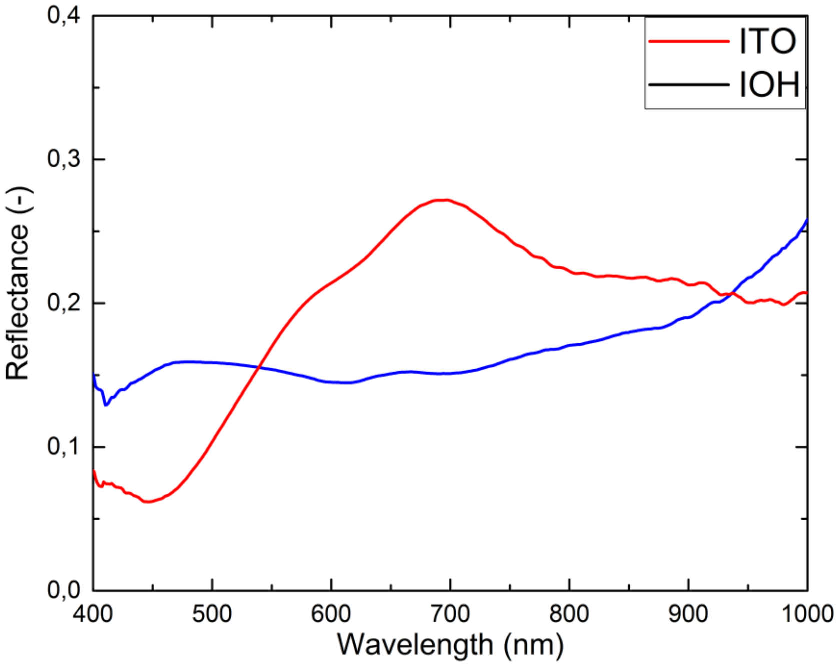

Figure 41: The reflectance for the ITO (red) and the IOH (black) layer

Figure 42 compares the J-V curves of the solar cell according to the initial and final design with both TCO's. It can be seen that using IOH as TCO has a huge impact on the performance of the device, both on the short circuit current and on the open circuit voltage. Table 10 lists the external parameters for the four different configurations. It can be seen that the impact of using IOH is on itself even bigger than the other deposition changes proposed in this work. There is a big difference in open circuit voltage between the cells using IOH and the cells using ITO. This difference could be due to a difference in band configuration of the a-Si top cell due to the TCO. Also, it is a possibility that the deposition of the ITO layer, in spite of the power gradient during deposition, damages the solar cell in such a way that the open circuit voltage drops. The large difference in V_{oc} however is not only caused by damage during the ITO deposition, since a large decrease in V_{oc} is not observed in the single junction cells and the c-Si/nc-Si tandem cell. However, the a-Si/nc-Si cells show a V_{oc} of around 1.0-1.1 Volts, while one would expect the V_{oc} of such cells to be higher, around 1.4-1.5 Volts. The previous master thesis, which used ITO as top layer, also reached V_{oc} values comparable to the ones shown here for the cells with ITO as TCO. This all together suggests that using ITO decreases the voltage of a multi-junction solar cell device with an a-Si top cell. Why and how this decrease in performance is caused is unknown, and it is suggested that future work on this subject should investigate the mechanism behind it. It is possible that the fact that ITO is a heavily doped n-type semiconductor is having an effect on energy band structure of the multijunction cell.

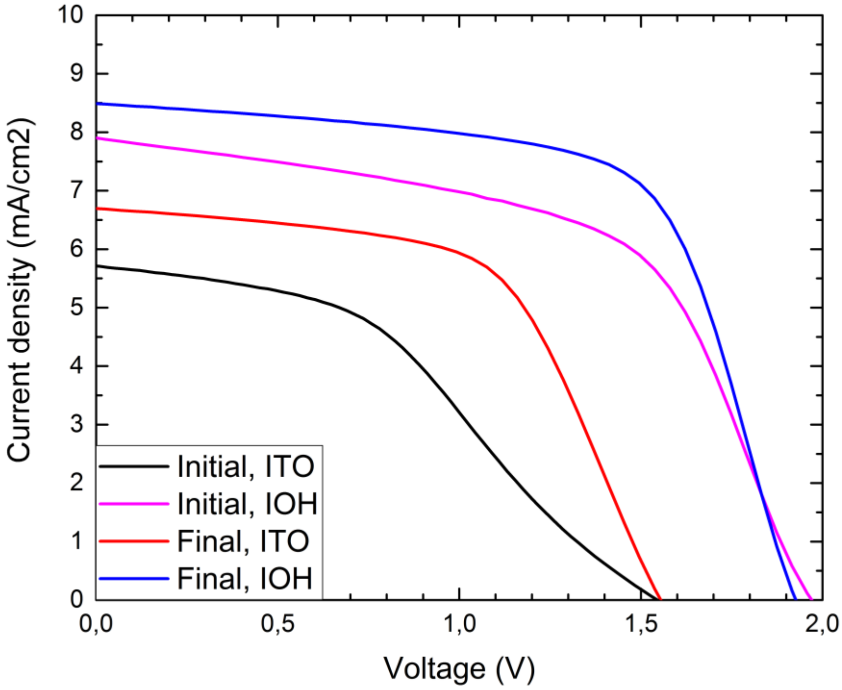

Figure 42: J-V curves for cells according to the initial and final design with ITO or IOH as top TCO.

Table 10: External parameters for all four triple junction solar cells

Sample	**Voc (V)**	**Jsc (mA/cm^2)**	**η (%)**	**FF(-)**	**Rs(Ωcm^2)**	**Rsh(Ωcm^2)**
Initial, ITO	1.54	5.7	3.6	0.42	266	1685
Initial, IOH	1.97	7.3	8.9	0.57	93	1127
Final, ITO	1.55	6.7	6.2	0.59	103	2929
Final, IOH	1.93	8.5	10.7	0.65	62	2722

The main difference between the cells made according initial and final deposition recipes with IOH on top lies in an improved fill factor, arising both from an increase in shunt resistance and a decrease in series resistance. The final fill factor of 0.65 is the highest result within this work, but still leaves room for improvement. In literature, it is reported that an IO:H/Ag front contact shows a high resistivity, possibly related to the formation of a thin AgO layer [96]. It is possible that the same mechanism plays a role here in the IO:H/Al interface. Protective layers of other metals more resistant to oxidation could be included to avoid this issue. In addition, the J_{sc}, and thus the operational current, could also be improved by improving the current matching of the device.

Finally, to get an indication of how the designed solar cell would operate in the final PV-electrolysis design the J-V curve is plotted together with the J-V curve of the IrO_x electrode that will be used as the electrode for the OER. This neglects possible overpotentials for the HER and other system resistivities, so we cannot claim that the crosspoint in this graph will be the operational point for the total system. An estimated 0.1 V of additional overpotential is taken into account. This includes an expected overpotential of 0.05 V for the HER for high quality electrodes at 10 mA/cm^2 [97], and 0.05 V of resistive losses [98]. Figure 43 shows an IrO_x counter electrode, accounting also for this overpotential, plotted with a dashed line, the operational current of the solar cell could be around 5 mA/cm^2, which would mean the system can reach a STH efficiency of 6.2%. This does not take into account the ratio between solar cell area and electrode area. When the cost of the catalyst is relatively high compared to the solar cell cost, for economically viable hydrogen production low catalyst area to solar cell area ratio is required [65]. This would mean that the IrO_x I-V curve would be less steep, and the solar cell performance would have to be improved to maintain a high STH efficiency.

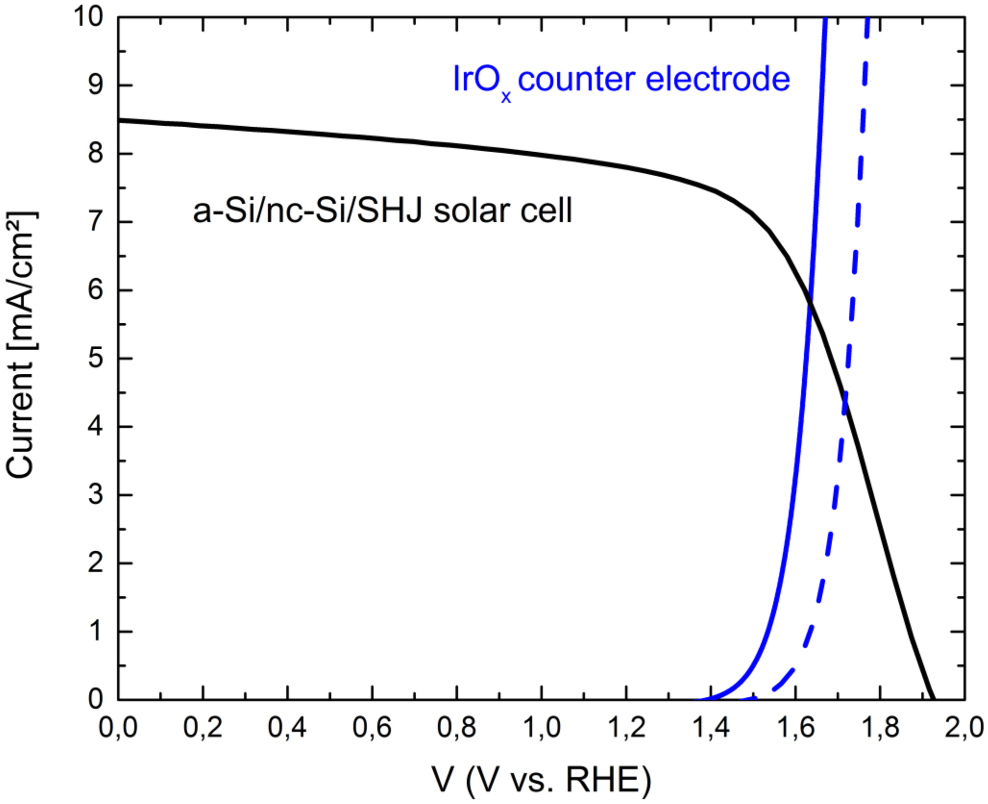

Figure 43: The J-V curve for the designed solar cell and the OER electrode (solid) and the OER electrode with 0.1 V overpotential added (dashed)

5. Conclusions and recommendations

5.1 Conclusions

In this report an a-Si:H/nc-Si:H/c-Si triple junction solar cell design has beed improved by investigating several parts of the device. Relevant parts of the cell are the two tunnel recombination junctions, the i-nc-Si middle absorber layer, the top p-nc-SiO_x layer and the TCO. The results of these experiments are combined into an improved design for the triple junction cell.

It was found that the improvement observed in superstrate cells using a p-contact layer/p-window layer with different CO_2/CH_4 ratios during deposition in combination with hydrogen passivation of the i-a-Si layer carries on to substrate a-Si cells. The fill factor of single junction a-Si cells on glass substrates increases from 0.55 to 0.65, the change in V_{oc} is under 0.05 Volts.

The thickness of the i-nc-Si absorber layer can be increased from 2800 to 3500 nm without negative consequences for the electrical performance of the nc-Si sub-cell. This increases the absorption of the nc-Si sub-cell in the red part of the spectrum, and can improve current matching of the total device slightly.

The performance of both TRJs can be improved. In the case of the TRJ between the a-Si and nc-Si sub-cells this is done by adding a 6 nm SiO_x layer which enables efficient recombination of charge carriers of both sub-cells. 6 nm is thin enough to limit the internal reflection caused by the different refractive indexes of SiO_x and Si. The thickness of the n-a-Si layer in this TRJ can be reduced from 30 to 20 nm to improve the electrical performance of the cell and reduce the parasitic losses associated with the n-layer. For the TRJ between the nc-Si and c-Si sub-cells it was found that increasing the dopant gas flow for the deposition of the n-a-Si layer improve the electrical performance of the cell, and also increase current collection. Using higher dopant gas flows has a detrimental effect on the i-nc-Si layer deposition.

The ITO that was used as a TCO throughout the experiment was compared to an IOH layer. It was found that IOH improves the optical performance of the device by a reduced reflection in the middle wavelength region, which increases the absorption in the nc-Si sub-cell. The electrical performance of the cells with IOH was also better than that of cells with ITO as front TCO. Although there is an influence of the resistivity of the TCO, the large improvement in V_{oc} of the final triple junction device cannot only be caused by IOH being a less resistive TCO. Why cells with ITO have such a low V_{oc} is unclear and this should be investigated further.

When the I-V curve of the final triple junction cell is compared with the IrO_x counter electrode, it is shown that water splitting is possible by using this triple junction design. The STH efficiency would be just around 6.2 %.In order to further improve this potential efficiency, some recommendations will be given.

5.2 Recommendations

The results show that using a triple junction solar cell design has the potential to be used efficiently in a direct PV-electrolysis setup. However, as stated in the conclusion, the STH efficiency is not high enough yet. There are several aspects of the solar cell that could be improved. A few of them will be named, with a short speculation on the possible effects.

One of the first issues arising from the experiments is the partial attachment of the nc-Si layer on top of the c-Si wafer. As long as this problem is not solved, it is not possible to produce a triple junction cell with a consistent performance. A possible solution is to slightly texture the top side of the c-Si wafer, so that enough roughness is introduced for the nc-Si deposition. This should be fine-tuned carefully. Not only is the passivation layer quality of the wafer, and thus the V_{oc}, related to the wafer texturing [46], but there is also another effect of substrate roughness on the nc-Si (sub-)cell quality. With increasing roughness the V_{oc} decreases due to an increase in defect density. A surface roughness suitable for stable layer deposition and high Vo_c needs to be found for that solution. Another option is to introduce graded doping in the a-Si layers between the c-Si and nc-Si sub-cell, so that the doping levels are high at the p-a-Si/n-a-Si interface to ensure good TRJ quality and low at the n-a-Si/i-nc-Si interface to give a better substrate.

Related to the defective nc-Si layers is that the shunt resistance of the solar cell is too low. The nc-Si cell is the current limiting sub-cell, so in the nc-Si layer shunt paths are present that reduce the operational current. This should also be taken into account while optimising the nc-Si deposition and the substrate roughness. In this optimisation special care should be taken towards the nc-Si crystallinity. The process must be optimised in such a way that the layer is deposited as close to the transition region towards amorphous silicon without actually going into this region.

A second issue is that the series resistance of the cell is still relatively high. It is possible that this has to do with the interface between the metal contact and the IOH layer. Testing a similar solution as proposed in literature, creating an IOH/ITO double layer, could solve this.

Another important issue is that the device is not current matched. Absorption in the nc-Si layer is too low, and as a result the c-Si wafer has a too high absorption. Hypothetically, if the current would be divided equally over the sub-cells the triple junction cell could reach a short circuit current of 12 mA/cm^2, while this is only 8.5 mA/cm^2. Light trapping techniques are needed to increase the absorption in the nc-Si layer. Two possible options are introducing an intermediate reflective layer between the nc-Si and c-Si cell, and to use a textured interface at the top. Texturing the top interface would increase the absorption in the a-Si layer as well, so a thinner a-Si layer should be used so that the current in the nc-Si layer can be improved. Another possibility is using a top a-Si cell with a slightly higher bandgap. This can potentially increase the V_{oc} of the triple junction device even further, while at the same time increasing the available light for the nc-Si middle cell.

Considering that the nc-Si layer is the layer where most issues arise in the triple junction cell configuration, one could also look into amorphous silicon germanium as an alternative absorption layer for the middle cell. The first advantage of a-SiGe is that the band gap lies in between that of a-Si and c-Si. The use of a layer with a medium band gap could increase the spectral utilisation, and increase the V_{oc} of the total device. The band gap can be fine-tuned by varying the Si:Ge ratio, and this also enables the fine-tuning of the absorption in the SiGe layer [99]. Furthermore, the growth problems observed with nc-Si in this project are not present for SiGe. This would take away the need for a slight texturing of the c-Si wafer, which is also a benefit for a high voltage solar cell device.

Bibliography

[1] Intergovernmental Panel on Climate Change, “Energy Systems,” in *Climate Change 2014, mitigation of climate change*, New York, Cambridge University Press, 2014, pp. 511-597.

[2] International Energy Agency, “World Energy Outlook 2016,” IEA Publications, Paris, 2016.

[3] International Energy Agency, “World Energy Outlook 2015,” IEA Publications, Paris, 2015.

[4] D.-L. Zhang and W.-Z. Zheng, “Diurnal Cycles of Surface Winds and Temperatures as Simulated by Five Boundary Layer Parameterizations,” *J. Appl. Meteor. Climatol.,* pp. 157-169, 1 January 2004.

[5] U.S. Energy Information Administration, “Monthly generator capacity factor data now available by fuel and technology,” 15 January 2014. [Online]. Available: https://www.eia.gov/todayinenergy/detail.php?id=14611&src=email. [Accessed 27 June 2017].

[6] F. Mulder, “Implications of diurnal and seasonal variations in renewable energy generation for large scale energy storage,” *J. Renewable Sustainable Energy,* April 2016.

[7] J. P. Barton and D. P. Infield, “Energy Storage and Its Use With Intermittent Renewable Energy,” *IEEE Transactions on Energy Conversion,* pp. 441-448, June 2004.

[8] J. A. Turner, “Sustainable Hydrogen Production,” *Science,* pp. 972-974, 13 Augustus 2004.

[9] R. v. d. Krol and M. Gratzel, Photoelectrochemical Hydrogen Production, New York: Springer Science and Business media, 2012.

[10] A. Zuttel, A. Remhof, A. Borgschulte and O. Friedrichs, “Hydrogen: the future energy carrier,” *Philosophical transactions of th royal society A,* vol. 368, no. 1923, pp. 3329-3342, 2010.

[11] A. J. Bard and M. A. Fox, “Artificial Photosynthesis: Solar Splitting of Water to Hydrogen and Oxygen,” *Accounts of Chemical Research,* pp. 141-145, March 1995.

[12] J. W. Ager, M. R. Shaner, K. A. Walczak, I. D. Sharp and S. Ardo, “Experimental demonstrations of spontaneous, solar-driven photoelectrochemical water splitting,” *Energy & Environmental Science,* vol. 8, pp. 2811-2824, 2015.

[13] J. Thorn, M. Neel, V. Donato, G. Bergreen, R. Davies and M. Beck, “Observing the quantum behavior of light in an undergraduate laboratory,” *Am. J. Phys,* vol. 72, no. 9, pp. 1210-1219, 2004.

[14] G. Kopp and J. L. Lean, “A new, lower value of total solar irradiance: Evidence and climate significance,” *Geophysical Research letters,* vol. 38, no. 1, 2011.

[15] C. Gueymard, D. Myers and K. Emery, “Proposed reference irradiance spectra for solar energy systems testing,” *Solar Energy,* vol. 73, no. 6, pp. 443-467, 2002.

[16] American Society for Testing and Materials (ASTM), “Reference Solar Spectral Irradiance: Air Mass 1.5,” National Renewable Energy Laboratory (NREL), 2004. [Online]. Available: http://rredc.nrel.gov/solar/spectra/am1.5/. [Accessed 07 11 2016].

[17] P. Rappaport, “The Photovoltaic effect and its Utilization,” *Solar Energy,* vol. 3, no. 4, pp. 8-18, 3.

[18] D. A. Neamen, Semiconductor Physics and Devices, New York: McGraw-Hill, 2003.

[19] G. Watson, “Introduction to Electronic Band Structure,” University of Delaware, 15 4 1999. [Online]. Available: http://www.physics.udel.edu/~watson/scen103/99s/clas0416.html. [Accessed 8 11 2016].

[20] Potenntial, “Power Semiconductors,” University of Tennessee Knoxville, 2015. [Online]. Available: http://potenntial.eecs.utk.edu/About.php?topic=PowerSemiconductors. [Accessed 10 07 2017].

[21] W. Shockley and H. J. Queisser, “Detailed balance Limit of Efficiency of p-n Junction solar cells,” *Journal of Applied Physics,* vol. 32, no. 3, pp. 510-519, 1961.

[22] S. Ruhle, “Tabulated values of the Schockley-Queisser limit for single junction solar cells,” *Solar Energy,* vol. 130, pp. 139-147, 2016.

[23] A. d. Vos, “Detailed balance limit of the efficiency of tandem solar cells,” *Journal of Physics D: Applied Physics,* vol. 13, pp. 839-846, 1980.

[24] M. A. Green, “Crystalline Silicon Solar Cells,” April 2001. [Online]. Available: http://www.univie.ac.at/photovoltaik/vorlesung/ss2013/unit9/silicon_solar_cells.PDF. [Accessed 09 June 2017].

[25] J. G. Fossum, “Physical Operation of Back Surface Field Silicon Solar Cells,” *IEEE Transactions on Electron Devices,* vol. 24, no. 4, pp. 322-325, 1977.

[26] R. Nave, “Bands for Doped Semiconductors,” Georgia State University, 1998. [Online]. Available: http://hyperphysics.phy-astr.gsu.edu/hbase/Solids/dsem.html. [Accessed 10 July 2017].

[27] T. Kirchartz, J. Bisquert, I. Mora-Sero and G. Garcia-Belmonte, “Classification of solar cells according to mechanisms of charge separation and charge collection,” *Physical chemistry chemical physics,* vol. 15, no. 6, pp. 4007-4014, 2015.

[28] A. Smets, K. Jager, O. Isabella, R. v. Swaaij and M. Zeman, Solar Energy, Cambridge: UIT Cambridge, 2016.

[29] A. Shah, P. Torres, R. Tscharner, N. Wyrsch and H. Keppner, “Photovoltaic Technology: The case for Thin-Film Solar Cells,” *Science,* vol. 285, no. 5428, pp. 692-698, 1999.

[30] U. Wurfel and A. Cuevas, “Charge Carrier Separation in Solar Cells,” *IEEE Journal of Photovoltaics,* vol. 5, no. 1, pp. 461-469, 2015.

[31] R. M. Miles, K. M. Hynes and I. Forbes, “Photovoltaic solar cells: An overview of state-of-the-art cell development and environmental issues,” *Progress in Crystal Growth and Characterization of Materials,* vol. 51, no. 1-3, pp. 1-42, 2005.

[32] H. Cotal, C. Fetzer, J. Boisvert, G. Kinsey, R. King, P. Hebert, H. Yoon and N. Karam, “III–V multijunction solar cells for concentrating photovoltaics,” *Energy & Environmental Science,* vol. 2, no. 1, pp. 174-182, 2009.

[33] C. S. Tao, J. Jiang and M. Tao, “Natural resource limitations to terawatt-scale solar cells,” *Solar Energy Materials and Solar Cells,* vol. 95, no. 12, pp. 3176-3180, 2011.

[34] Fraunhofer ISE, PSE AG, “Photovoltaics Rapport,” 17 November 2016. [Online]. Available: https://www.ise.fraunhofer.de/content/dam/ise/de/documents/publications/studies/Photovoltaics-Report.pdf. [Accessed 09 June 2017].

[35] A. Feltrin and A. Freundlich, “Material considerations for terawatt level deployment of photovoltaics,” *Renewable Energy,* vol. 33, no. 2, pp. 180-185, 2008.

[36] A. G. Aberle, “Thin-film Solar Cells,” *Thin Solid Films,* vol. 517, no. 17, pp. 4706-4710, 2009.

[37] L. L. Kazmerski, “Solar photovoltaics R&D at the tipping point: A 2005 technology overview,” *Journal of Electron Spectroscopy and Related Phenomena,* vol. 150, pp. 105-135, 2006.

[38] S. N. Agbo, “Growth and Characterization of Thin Film Nanocrystalline Silicon Materials and Solar Cells,” 2012.

[39] D. Staebler and C. Wronski, “Reversible conductivity changes in discharge-produced amorphous

Si," *Applied Physics Letters,* vol. 31, no. 4, pp. 292-294, 1977.

[40] F. Hamelmann, J. Weicht and G. Behrens, "Light-Induced Degradation of Thin Film Silicon Solar Cells," *Journal of Physics: Conference Series,* vol. 682, 2016.

[41] B. Yan, G. Yue, L. Sivec, C.-S. Jiang, Y. Yan, K. Alberi, J. Yang and S. Guha, "On the bandgap of hydrogenated nanocrystalline silion thin films," in *Photovoltaic Specialists Conference (PVSC), 35th IEEE*, Honolulu, 2010.

[42] A. Madhavan, "Alternative designs for nanocrystalline silicon solar cells," Ioha State University, 2009.

[43] O. Vetterl, F. Finger, R. Carius, P. Hapke, L. Houben, O. Kluth, A. Lambertz, A. Muck, B. Rech and H. Wagner, "Intrinsic microcrystalline silicon: A new material for photovoltaics," *Solar Energy Materials and Solar Cells,* vol. 62, no. 1, pp. 97-108, 2000.

[44] L. V. Mercaldo, I. Usatii and P. Delli Veneri, "Advances in Thin-Film Si Solar Cells by Means of SiOx Alloys," *energies,* vol. 9, no. 3, pp. 218-231, 2016.

[45] M. Taguchi, A. Yano, S. Tohoda, K. Matsuyama, N. Yuya, T. Nishiwaki, K. Fujita and E. Maruyama, "24.7% Record Efficiency HIT Solar Cell on Thin Silicon Wafer," *IEEE Journal of photovoltaics,* vol. 4, no. 1, pp. 96-99, 2012.

[46] A. Descoeudres, Z. C. Holman, L. Barraud, S. Morel, S. D. Wolf and C. Ballif, ">21% Efficient Silicon Heterojunction Solar Cells on n- and p- Type Wafers Compared," *IEEE Journal of Photovoltaics,* vol. 3, no. 1, pp. 83-89, 2013.

[47] S. D. Wolf, A. Descoeudres, Z. C. Holman and C. Ballif, "High-efficiency Silicon Heterojunction Solar Cells: A Review," *Green,* vol. 2, pp. 7-24, 2012.

[48] K. Masuko, M. Shigematsu, T. Hashiguchi, D. Fujishima, M. Kai, N. Yoshimura, T. Yamaguchi, Y. Ichihasi, T. Mishima, N. Matsubara, T. Yamanishi, T. Takahama, M. Taguchi, E. Maruyama and S. Okamoto, "Achievement of more than 25% Conversion Efficiency with Crystalline Silicon Heterojunction Solar Cell," *IEEE Journal of Photovoltaics,* vol. 4, no. 6, pp. 1433-1435, 2014.

[49] H.-P. Wang, A.-C. Li, T.-Y. Lin and J.-H. He, "Concurrent improvement in optical and electrical characteristics by using inverted pyramidal array structures toward efficient Si heterojunction solar cells," *Nano Energy,* vol. 23, pp. 1-6, 2016.

[50] A. de Vos, "Detailed balance limit of the efficiency of tandem solar cells," *Journal of Physics D: Applied Physics,* vol. 13, no. 5, pp. 839-846, 1980.

[51] M. A. Green, K. Emery, Y. Hishikawa, W. Warta, E. D. D. Dunlop, D. H. Levi and A. W. Ho-Baillie, "Solar cell efficiency tables (version 49)," *Progress in photovoltaics,* vol. 25, no. 1, pp. 3-13, 2017.

[52] Y. Hamakawa and S. K. Deb, "Recent Advances and Future Opportunities for Thin-Film Solar Cells," in *Thin- Film Solar Cells: Next Generation Photovoltaics and its Applications*, Berlin, Springer-Verlag, 2004, pp. 18-19.

[53] Solar Junction, "Technology," Solar Junction Corporation, 2016. [Online]. Available: http://www.sj-solar.com/technology/. [Accessed 10 June 2017].

[54] S. S. Hegedus, F. Kampas and J. Xi, "Current transport in amorphous silicon n/p junction and their application as tunnel junctions in tandem solar cells," *Applied Physics Letters,* vol. 67, no. 6, pp. 813-815, 1995.

[55] B. Bills, X. Liao, D. W. Galipeau and Q. H. Fan, "2012," *IEEE Transactions on Electron Devices,* vol. 59, no. 9, pp. 2327-2330, 2012.

[56] Y. Lee, V. A. Dao, S. M. Iftiquar, S. Kim and J. Yi, “Current transport studies of amorphous n/p junctions and its application in a-Si:H/HIT-type tandem cells,” *Progress in Photovoltaics,* vol. 24, pp. 52-58, 2016.

[57] F. A. Rubinelli, J. K. Rath and R. E. I. Schropp, “Microcrystalline n-i-p tunnel junction in a-Si:H/a-Si:H tandem cells,” *Journal of Applied Physics,* vol. 89, no. 7, pp. 4010-4018, 2001.

[58] E. Zoulias, E. Varkaraki, N. Lymberopoulos, C. N. Christodoulou and G. N. Karagiorgis, “A review on water electrolysis,” *TCJST,* vol. 4, no. 2, pp. 41-71, 2004.

[59] K. W. Harrison, R. Remick and G. D. Martin, “Hydrogen Production: Fundamentals and Cas Study,” in *World Hydrogen Energy Conference*, Essen, 2010.

[60] K. Zeng and D. Zhang, “Recent progress in alkaline water electrolysis for hydrogen production,” *Progress in Energy and Combustion Science,* vol. 36, no. 1, pp. 307-326, 2010.

[61] M. G. Walter, E. L. Warren, J. R. McKone, S. W. Boettcher, Q. Mi, E. A. Santori and N. S. Lewis, “Solar Water Splitting Cells,” *Chemical Reviews,* vol. 110, no. 11, pp. 6446-6473, 2010.

[62] F. E. Osterloh and B. A. Parkinson, “Recent developments in solar water splitting photocatalysis,” *MRS Bulletin,* vol. 36, no. 1, pp. 17-22, 2011.

[63] F. F. Abdi, L. Han, A. H. M. Smets, M. Zeman, B. Dam and R. v. d. Krol, “Efficient solar water splitting by enhanced charge separation in a bismuth vanadate silicon tandem photoelectrode,” *Nature communications,* vol. 4, no. 2195, 2013.

[64] O. Khaselev and J. A. Turner, “A Monolithic Photovoltaic-Photoelectrochemical Device for Hydrogen Production via Water Splitting,” *Science,* vol. 280, no. 5362, pp. 425-427, 1998.

[65] C. A. Rodriguez, M. A. Modestino, D. Psaltis and C. Moser, “Design and cost considerations for practical solar-hydrogen generators,” *Energy & Environmental Science,* vol. 7, no. 10, pp. 3828-3835, 2014.

[66] J.-W. Schuttauf, M. A. Modestino, E. Chinello, D. Lambelet, A. Delfino, D. Domine, A. Faes, M. Despeisse, J. Bailat, D. Psaltis, C. Moser and C. Ballif, “Solar-to-Hydrogen Production at 14.2% Efficiency with Silicon Photovoltaics and Earth-Abundant Electrocatalysts,” *Journal of the Electrochemical Society,* vol. 163, no. 10, pp. 1177-1181, 2016.

[67] M. Falkenberg, “A Multi-Junction Solar Cell for Water Splitting: Development of an a-Si:H/nc-Si:H/SHJ triple junction solar cell,” 2016.

[68] D. Deligiannis, S. Alivizatos, A. Ingenito, D. Zhang, M. v. Sebille, R. A. C. M. M. v. Swaaij and M. Zeman, “Wet-chemical treatment for improved surface passivation of textured silicon heterojunction solar cells,” *Energy Procedia,* vol. 55, pp. 197-202, 2014.

[69] E. B. Wisborg, “Plasma-Enhanced Chemical Vapour Deposition,” 12 March 2014. [Online]. Available: http://folk.uio.no/yurig/Nanotechnology/Student_presentations/2014/Emil%20Wisborg%20-%20PECVD.pdf. [Accessed 01 June 2017].

[70] A. El amrani, I. Menous, L. Mahiou, R. Tadjine, A. Touati and A. Lefgoum, “Silicon nitride film for solar cells,” *Renewable Energy,* vol. 33, no. 10, pp. 2289-2293, 2008.

[71] G. Dingemans, M. C. M. v. d. Sanden and W. M. M. Kessels, “Influence of the Deposition Temperature on the c-Si Surface Passivation by Al2O3 Films Synthesized by ALD and PECVD,” *Electrochemical and Solid-State Letters,* vol. 13, no. 3, pp. 76-79, 2010.

[72] J. B. Gibson, A. N. Goland, M. Milgram and G. H. Vineyard, “Dynamics of Radiation Damage,”

Physical Review, vol. 120, no. 4, pp. 1229-1253, 1960.

[73] M-System co., “newsletter,” M-System , April 2010. [Online]. Available: http://www.m-system.co.jp/newsletter/182/clip_contents.html. [Accessed 06 Juni 2017].

[74] D. Zhang, A. Tavakoliyaraki, Y. Wu, R. A. C. M. M. v. Swaaij and M. Zeman, “Influence of ITO deposition and post ainnealing on HIT solar cell structures,” *Energy Procedia,* vol. 8, pp. 207-213, 2011.

[75] B. Macco, H. C. M. Knoops and W. M. M. Kessels, “Electron Scattering and Doping Mechanisms in Solid-Phase-Crystallized In2O3:H Prepared by Atomic Layer Deposition,” *Applied Materials & Interfaces,* vol. 7, pp. 16723-16729, 2015.

[76] AJA, “What is Thermal Evaporation,” AJA international inc. , 2011. [Online]. Available: http://www.ajaint.com/what-is-e-beam-evaporation.html. [Accessed 06 June 2017].

[77] AJA, “What is e-beam evaporation,” AJA international inc., 2011. [Online]. Available: http://www.ajaint.com/what-is-e-beam-evaporation.html. [Accessed 06 June 2017].

[78] Power Systems Design, “Solar Battery Charger,” Power Systems Corporation, 2017. [Online]. Available: https://www.powersystemsdesign.com/articles/solar-battery-charger/28/5809. [Accessed 06 June 2017].

[79] National Instruments, “Photovoltaic Cell I-V Characterization Theory and LabVIEW Analysis Code,” National Instruments Nederland, 10 May 2012. [Online]. Available: http://www.ni.com/white-paper/7230/en/. [Accessed 07 June 2017].

[80] Wacom, “Solar Simulator,” Wacom Electric Co. LTD, 2012. [Online]. Available: http://www.wacom-ele.co.jp/en/products/solar/super/. [Accessed 07 June 2017].

[81] C. Honsberg and S. Bowden, “Current losses due to recombination,” PV education, 2013. [Online]. Available: http://www.pveducation.org/pvcdrom/design/current-losses-due-to-recombination. [Accessed 04 June 2017].

[82] H. Tan, P. Babal, M. Zeman and A. H. M. Smets, “Wide bandgap p-type nanocrystalline silicon oxide as window layer for high performance thin-film silicon multi-junction solar cells,” *Solar Energy Materials and Solar Cells,* vol. 132, pp. 597-605, 2015.

[83] B. Vet, “Improvement of a-Si:H devices by analysis, simulation and experiment,” 2014.

[84] S. Klein, T. Repmann and T. Brammer, “Microcrystalline silicon films and solar cells deposited by PECVD and HWCVD,” *Solar Energy,* vol. 77, no. 6, pp. 893-908, 2004.

[85] K. Kim and Y. Kuo, “Influence of pin Amorphous Silicon Stack Deposition Sequence on Solar Cell performance and Degradation,” *Journal of Solid State Science and Technology,* vol. 6, no. 1, pp. 29-33, 2017.

[86] J. Bailat, D. Domine, R. Schluchter, J. Steinhauser, S. Fay, F. Freitas, C. Bucher, L. Feitknecht, X. Niquille, T. Tscharner, A. Shah and C. Ballif, “HIgh-efficiency p-i-n microcrystalline and micromorph thin film silicon solar cells deposited on LPCVD ZNO coated glass substrates,” *Conference Record of the 2006 IEEE 4th World Conference on Photovoltaic Energy Conversion,* vol. 2, pp. 1533-1536, 2006.

[87] M. Python, E. Vallat-Sauvain, J. Bailat, D. Domine, L. Fesquet, A. Shah and C. Ballif, “Relation between substrate surface morphology and microcrystalline silicon solar cell performance,” *Journal of Non-Cyrstalline Solids,* vol. 354, no. 19-25, pp. 2258-2262, 2008.

[88] M. Python, O. Madani, D. Domine, F. Meillaud, E. Vallat-Sauvain and C. Ballif, “Influence of the substrate geometrical parameters on microcrystalline silicon growth for thin-film solar cells,” *Solar*

Energy Materials and Solar Cells, vol. 2009, no. 10, pp. 1714-1720, 2009.

[89] H. Sakahi, T. Yoshida, S. Fujikake, Y. Ichikawa, A. Ueda, O. Ishiwata and M. Nagano, “Effects of the surface morphology of transparent electrode on film deposition and photovoltaic performance of a-SI:H solar cells,” *Journal of Non-Crystalline Solids,* vol. 115, no. 1-3, pp. 198-200, 1989.

[90] S. Hanni, G. Bugnon, G. Parascandolo, M. Boccard, J. Escarre, M. Despeisse, F. Meillaud and C. Ballif, “High-efficiency microcrystalline silicon single-junction solar cells,” *Progress in Photovoltaics,* vol. 21, no. 5, pp. 821-826, 2013.

[91] H. Tan, E. Psomadaki, O. Isabella, M. Fischer, B. Pavel, R. Vasudevan, M. Zeman and A. H. M. Smets, “Micro-textures for efficient light trapping and improved electrical performance in thinfilm,” *Applied Physics Letters,* vol. 103, no. 10, 2013.

[92] S. Ishizuka, K. Sakurai, A. Yamada, K. Matsubara, P. Fons, K. Iwata, S. Nakamura, Y. Kimura, T. Baba, H. Nakanishi, T. Kojima and S. Niki, “Fabrication of wide-gap Cu(In1−xGax)Se2 thin film solar cells: a study on the correlation of cell performance with highly resistive i-ZnO layer thickness,” *Solar Energy Materials and Solar Cells,* vol. 87, no. 1, pp. 541-548, 2005.

[93] J. L. Muench, J. Kruuv and J. R. Lepock, “A two-step Reversible-Irreversible Model Can Account for a Negative Activation Energy in an Arrhenius Plot,” *Cryobiology,* vol. 33, no. 2, pp. 253-259, 1996.

[94] L. E. Revell and B. E. Williamson, “Why are some reactions slower at high temperatures,” *Journal of Chemical Education,* vol. 90, no. 8, pp. 1024-1027, 2013.

[95] V. Smirnov, A. Lambertz, B. Grootoonk, R. Carius and F. Finger, “Microcrystalline silicon oxide (μc-SiOx:H) alloys: A versatile material for application in thin film silicon single and tandem junction solar cells,” *Journal of Non-Crystalline Solids,* vol. 358, no. 17, pp. 1954-1957, 2012.

[96] L. Barraud, Z. C. Holman, N. Badel, P. Reiss, A. Descoeudres, C. Battaglia, C. De Wolf and C. Ballif, “Hydrogen-doped indium oxide/indium tin oxide bilayers for high-efficiency silicon heterojunction solar cells,” *Solar Energy Materials & Solar Cells,* vol. 115, pp. 151-156, 2013.

[97] C. C. L. McCrory, S. Jung, I. M. Ferrer, S. M. Chatman, J. C. Peters and T. F. Jaramillo, “Benchmarking Hydrogen Evolving Reaction and Oxygen Evolving Reaction Electrocatalysts for Solar Water Splitting Devices,” *Journal of the American Chemical Society,* vol. 137, no. 13, pp. 4347-4357, 2015.

[98] M. R. Singh, K. Papadantonakis, C. Xiang and N. S. Lewis, “An electrochemical engineering assessment of the operational conditions and constraints for solar-driven water-splitting systems at near-neutral pH,” *Energy & Environmental Science,* vol. 8, pp. 2760-2767, 2015.

[99] X. Deng, X. Liao, S. Han, H. Povolny and P. Agarwal, “Amorphous silicon and silicon germanium materials for high-efficiency triple-junction solar cells,” *Solar Energy Materials and Solar Cells,* vol. 62, no. 1-2, pp. 89-95, 2000.

Appendix

Layer	Gas flow SiH4 (sccm)	Gas flow B2H6 (sccm) 2% in H2	Gas flow B2H6 (sccm) 200ppm in H2	Gas flow PH3 (sccm) 2% in H2	Gas flow H2 (sccm)	Gas flow Ar (sccm)	Gas flow CO2 (sccm)	process pressure P (mbar)	eletrode distance Ed (mm)	Substrate temperature T °C	forward power Pf (W)	Load Capacitor CL	Tune Capacitor CT
p-a-Si	20	1						0.7		180	2.3	70	33
n-a-Si	40			11				0.6		180	2	52	33
i-a-Si	40							0.7		180	1.6	56	27
AZO						20		2.5		400	400	17.9	48.2
n-a-Si:H	40			11				0.6	14	300	4	13.4	67
i-nc-Si seed	1.2				120			4	11	200	40	10.9	10.4
i-nc-Si	3.4				120			4	11	200	40	10.9	10.4
p-nc-SiOx:H	0.8		10		170		1.6	2.2	14	300	12	11.2	68.5
n-nc-SiOx	1			1.2	100		1.6	1.5	21	300	11	13.2	68.2
i-a-Si:H	40							0.7	14	300	3.1	16.6	64.5
p-SiOx:H	0.8		20		170		2.3	2.2	14	300	12	11.4	70
IOH						40		0.0057		25	40		
ITO graded layer						40		0.0018		60	50		
ITO graded layer						40		0.0018		70	50		
ITO graded layer						40		0.0018		80	50		
ITO graded layer						40		0.0018		90	50		
ITO graded layer						40		0.0018		100	50		
ITO graded layer						40		0.0018		110	50		
ITO graded layer						40		0.0018		110	100		